

Differentiating Formation Models with New Dynamical Masses for the PDS 70 Protoplanets

David Trevascus^{1,2}, Sarah Blunt³, Valentin Christiaens^{4,5}, Elisabeth Matthews¹, Iain Hammond⁶, Wolfgang Brandner¹, Jason Wang³, Sylvestre Lacour^{7,8}, Arthur Vigan⁹, William O. Balmer^{10,11}, Mickael Bonnefoy¹², Remo Burn¹, Gaël Chauvin^{1,13}, Raffaele Gratton¹⁴, Mathis Houllé^{12,13}, Sasha Hinkley¹⁵, Jens Kammerer⁸, Laura Kreidberg¹, Gabriel-Dominique Marleau^{1,16,17}, Dino Mesa¹⁴, Gilles Otten¹⁸, Mathias Nowak⁷, Emily Rickman¹⁹, Joel Sanchez-Bermudez²⁰, Jonas Sauter^{1,2}

¹ Max-Planck-Institut für Astronomie, Königstuhl 17, 69117 Heidelberg, Germany

² Universität Heidelberg, Grabengasse 1, 69117 Heidelberg, Germany

³ Center for Interdisciplinary Exploration and Research in Astrophysics (CIERA) and Department of Physics and Astronomy, Northwestern University, Evanston, IL 60208, USA

⁴ Institute of Astronomy, KU Leuven, Celestijnenlaan 200D, Leuven, Belgium

⁵ Space sciences, Technologies & Astrophysics Research (STAR) Institute, Université de Liège, Allée du Six Août 19c, B-4000 Sart Tilman, Belgium

⁶ School of Physics and Astronomy, Monash University, Clayton, VIC 3800, Australia

⁷ LESIA, Observatoire de Paris, Université PSL, CNRS, Sorbonne Université, Université Paris Cité, 5 place Jules Janssen, 92195 Meudon, France

⁸ European Southern Observatory (ESO), Karl-Schwarzschild-Straße 2, 85748 Garching, Germany

⁹ Université Aix-Marseille, CNRS, CNES, LAM, Marseille, France

¹⁰ Department of Physics & Astronomy, Johns Hopkins University, 3400 N. Charles Street, Baltimore, MD 21218, USA

¹¹ Space Telescope Science Institute (STScI), 3700 San Martin Drive, Baltimore, MD 21218, USA

¹² Université Grenoble Alpes, CNRS, IPAG, 38000 Grenoble, France

¹³ Laboratoire Lagrange, Université Côte d'Azur, CNRS, Observatoire de la Côte d'Azur, 06304 Nice, France

¹⁴ INAF – Osservatorio Astronomico di Padova, Vicolo dell'Osservatorio 5, 35122 Padova, Italy

¹⁵ University of Exeter, Physics Building, Stocker Road, Exeter EX4 4QL, UK

¹⁶ Fakultät für Physik, Universität Duisburg-Essen, Lotharstraße 1, 47057 Duisburg, Germany

¹⁷ Physikalisches Institut, Universität Bern, Gesellschaftsstr. 6, 3012 Bern, Switzerland

¹⁸ Academia Sinica, Institute of Astronomy and Astrophysics, 11F Astronomy-Mathematics Building, NTU/AS campus, No. 1, Section 4, Roosevelt Rd., Taipei 10617, Taiwan

¹⁹ European Space Agency (ESA), ESA Office, STScI, 3700 San Martin Drive, Baltimore, MD 21218, USA

²⁰ Instituto de Astronomía, Universidad Nacional Autónoma de México, Apdo. Postal 70264, Ciudad de México 04510, Mexico

Received January 28, 2025; accepted ??

ABSTRACT

Hot- and cold-start planet formation models predict differing luminosities for the young, bright planets that direct imaging surveys are most sensitive to. However, precise mass estimates are required to distinguish between these models observationally. The presence of two directly imaged planets, PDS 70 *b* and *c*, in the PDS 70 protoplanetary disk provides us a unique opportunity for dynamical mass measurements, since the masses for these planets are currently poorly constrained. Fitting orbital parameters to new astrometry of these planets, taken with VLTI/GRAVITY in the *K* band, we find 2σ dynamical upper mass limits of $4.9 M_{\text{Jup}}$ for *b* and $13.6 M_{\text{Jup}}$ for *c*. Adding astrometry from the newly proposed planet candidate PDS 70 *d* into our model, we determine 2σ dynamical upper mass limits of $5.3 M_{\text{Jup}}$, $7.5 M_{\text{Jup}}$ and $2.2 M_{\text{Jup}}$ for *b*, *c*, and the candidate *d* respectively. However, *N*-body analysis of the orbits fit in this case suggest that the inclusion of *d* makes the system unstable. Using the upper mass limits for *b* and *c* we rule out the coldest-start formation models for both planets, calculating minimum post-formation entropies (S_i) of $9.5 k_{\text{B}}$ /baryon and $8.4 k_{\text{B}}$ /baryon respectively. This places PDS 70 *b* and *c* on the growing list of directly-imaged planets inconsistent with cold-start formation.

Key words. Planets and satellites: dynamical evolution and stability – Planets and satellites: formation – Techniques: high angular resolution – Astrometry – Planets and satellites: individual: PDS 70 *b* Planets and satellites: individual: PDS 70 *c*

1. Introduction

The sensitivity of direct-imaging surveys is highly dependent on the assumed model of planet formation. Hot-start (e.g., Baraffe et al. 2003; Phillips et al. 2020), warm-start (e.g., Spiegel & Burrows 2012; Linder et al. 2019), and cold-start (e.g., Marley et al. 2007; Fortney et al. 2008) planet evolution models all assume

different post-formation entropies (S_i), leading to differing luminosity predictions for young planets $\lesssim 100$ Myr old, which are the typical targets of these surveys.

Planet masses are traditionally inferred from evolutionary models (e.g., Bowler 2016), but these mass estimates are often poorly constrained and dependent upon the choice of model. However, dynamical mass estimation can provide model-

independent planet masses with much stronger constraints, such as for β Pic b and c (Brandt et al. 2021a), HR 8799 e (Brandt et al. 2021b; Zurlo et al. 2022) and AF Lep b (Balmer et al. 2024). Moreover, precise dynamical mass estimates, in combination with planet ages and luminosities, can be used to constrain S_i for these planets and therefore rule out certain hot-, warm- or cold-start models (Marleau & Cumming 2014).

PDS 70 is a young (5.4 ± 1.0 Myr, Müller et al. 2018) system containing two directly-imaged planets, PDS 70 b (Keppler et al. 2018) and PDS 70 c (Haffert et al. 2019), orbiting within a protoplanetary disk (Riaud et al. 2006). While the age of this system would allow us to differentiate between hot- and cold-start formation, these planets present a particular challenge for dynamical mass fitting, since the currently available astrometry covers a relatively small fraction of their total orbital periods. Wang et al. (2021) determined a 2σ upper mass limit for b of $10 M_{\text{Jup}}$, but were unable to constrain the mass of c within their uniform prior of $1\text{--}15 M_{\text{Jup}}$. Given its ability to achieve astrometric precisions down to $50 \mu\text{as}$ (GRAVITY Collaboration et al. 2017, 2020), the GRAVITY instrument on the Very Large Telescope Interferometer (VLTI) is well placed to provide the precise relative astrometry necessary for dynamical mass estimates in exoplanetary systems (e.g., Balmer et al. 2024).

Recently, Christiaens et al. (2024) reported the detection of a point-like signal located near the outer edge of the PDS 70 inner disk compatible with the presence of a third protoplanet in the system. This new planet candidate, referred to from here as PDS 70 d, is consistent with similar features observed with VLT/SPHERE high-contrast imaging by Mesa et al. (2019) and re-reductions of VLT/SINFONI, VLT/NaCo and VLT/SPHERE imaging (Hammond et al. 2025). However, current observations do not eliminate the possibility that this signal belongs to a dusty feature of the protoplanetary disc.

In this paper, we use new GRAVITY observations of PDS 70 b and c to fit orbital parameters to these planets, including updated dynamical mass estimates. The observations are described in Section 2. In Section 3.1 we fit orbital parameters to a two-planet system described by astrometry from b and c only. In Section 3.2 we fit orbital parameters to a three-planet system described by astrometry from b, c and the candidate d. In Section 4 we use our dynamical mass estimates from both scenarios to constrain S_i for these planets, and determine which of the hot-, warm-, and cold-start evolutionary models are consistent with these masses. We discuss our results in Section 5 and our conclusions are given in Section 6.

2. Observations and Data Reduction

2.1. GRAVITY Observations

The new astrometric measurements presented in this paper were obtained between Jan 2021 and Feb 2022 with the GRAVITY instrument (GRAVITY Collaboration et al. 2017) and the four 8m Unit Telescopes (UTs) of ESO’s VLTI. The star PDS 70 A itself served as the visual natural guide star for the adaptive optics and as the K-band fringe tracking reference source. We collected data using the K-band medium resolution mode ($R \approx 500$). The observing set-up followed the strategy outlined in Nowak et al. (2020) and Wang et al. (2021). Table 1 gives an overview on the observing dates, integration times on each planet, and atmospheric conditions. In our analysis (see Section 3) we combined this new data with GRAVITY astrometry from Wang et al. (2021).

2.2. Reduction of Relative Astrometry

The data were reduced using the standard GRAVITY pipeline (Lapeyrère et al. 2014) resulting in “astroreduced” OIFITS (Optical Interferometry FITS) files. Subsequent analysis used the Python scripts cleanGRAVITY and exoGRAVITY (Nowak et al. 2020) to deduce the relative astrometry between the planet and the star. The resulting measurements are reported in Table 2. Typical uncertainties in the relative position of PDS 70 c amount to a few $100 \mu\text{as}$. For PDS 70 b, the analysis of the 2021-01-07 data set resulted in uncertainties on the combined relative astrometry larger than 6 mas. We attribute this to a combination of relatively short total integration time, varying and unfavourable observing conditions, and the challenge of observing a planet separated by less than three times the single UT K-band diffraction limit from its host star. Given the large uncertainty, we ignored this epoch in the subsequent analysis. The 2022-02-21 data set on PDS 70 b constitutes a four times longer observing sequence, with 2/3 of the data obtained in good to very good observing conditions, resulting in relative astrometry with uncertainties of $\lesssim 1$ mas. All of the astrometry for PDS 70 c was obtained in good observing conditions and so none of it needed to be discarded.

3. Orbital Dynamics

3.1. Orbital Fitting with MCMC

We fit orbital parameters to PDS 70 b and c with the *orbitize* package (version 3.0.0; Blunt et al. 2020) using a combination of our new GRAVITY astrometry, astrometry from a new reduction of VLT/SINFONI data (described in Appendix A), and literature astrometry from Gemini/NICI (Keppler et al. 2018), VLT/NaCo (Keppler et al. 2018), VLT/SPHERE/IRDIS (Keppler et al. 2018; Müller et al. 2018; Mesa et al. 2019; Wahhaj et al. 2024), VLT/SINFONI (Christiaens et al. 2019), VLT/MUSE (Haffert et al. 2019), Keck/NIRC2 (Wang et al. 2020), VLT/GRAVITY (Wang et al. 2021), JWST/NIRISS (Blakely et al. 2024), JWST/NIRCam (Christiaens et al. 2024) and MagAO-X (Close et al. 2025). For a complete list of the astrometry used from the literature, see Table B.1 in Appendix B.

orbitize! uses the parallel-tempered affine-invariant Markov chain Monte Carlo (MCMC) sampler *ptemcee* (Foreman-Mackey et al. 2013; Vousden et al. 2016) for orbital fitting. Parallel-tempered MCMC utilizes multiple Markov chains at different “temperatures”. With increasing temperature, the posterior distribution asymptotes to the prior, preventing the sampler from becoming stuck within well separated modes. We used 20 temperatures, with 1000 walkers at each temperature and 20,000 steps per walker. Convergence was assessed by visual inspection of the walker chains. In order to remove burn-in, the last 10,000 steps from each walker (10 million parameter sets in total) were used to form the posterior probability distribution.

We fit the following orbital parameters for each planet: semi-major axis (a), eccentricity (e), inclination (i), argument of periastron (ω), longitude of the ascending node (Ω), epoch of periastron in units of the fractional orbital period (τ), and mass (M). Inclinations above 90 degrees refer to clockwise orbits, while inclinations below 90 degrees refer to counter-clockwise orbits. MJD 58,849 (2020-01-01) was used as the reference epoch for τ for both planets. Subscripts on the parameters indicate whether they belong to PDS 70 b or c. We also fit the stellar mass (M_*) and system parallax.

The priors used for each parameter are listed in Table 3. The priors for all the planetary parameters, with the exception

Table 1. Observing log of the new GRAVITY astrometric measurements reported in this paper. MJD corresponds to the halftime of each observing sequence.

Date	MJD	Planet	DIT/NDIT/NEXP	Airmass	Seeing [arcsec]	τ_0 [ms]	Proposal ID
2021-01-07 ^a	59221.37	<i>b</i>	100s/4/3	1.20–1.38	0.70–1.21	4.6–6.4	1104.C-0651
2021-01-08	59222.34	<i>c</i>	100s/4/5	1.26–1.69	0.37–0.65	4.8–8.6	1104.C-0651
2021-03-28	59301.24	<i>c</i>	100s/4/4	1.05–1.09	0.66–0.94	3.8–5.0	105.209D
2021-03-29	59302.25	<i>c</i>	100s/4/4	1.04–1.07	0.42–0.56	5.4–7.1	105.209D
2021-04-03	59307.23	<i>c</i>	100s/4/4	1.04–1.08	0.48–0.76	4.1–7.1	105.209D
2021-05-29	59363.10	<i>c</i>	100s/4/8	1.04–1.08	0.48–0.98	3.3–6.3	105.209D
2021-05-31	59365.03	<i>c</i>	100s/4/4	1.07–1.17	0.59–0.79	2.4–4.8	105.209D
2022-02-21	59631.28	<i>b</i>	100s/4/12	1.05–1.53	0.57–1.41	1.9–9.1	1104.C-0651
2022-02-21	59631.28	<i>c</i>	100s/4/7	1.07–1.33	0.61–1.23	3.3–8.5	1104.C-0651

Notes. ^(a) Data of lower quality. This epoch has been ignored in the subsequent analysis.

Table 2. Astrometry of PDS 70 b and c relative to the central star.

	MJD (days)	$\Delta R.A.$ (mas)	$\sigma_{\Delta R.A.}$ (mas)	$\Delta Decl.$ (mas)	$\sigma_{\Delta Decl.}$ (mas)	ρ
<i>b</i>	59631.28	111.14	1.0	−115.78	0.83	−0.58
<i>c</i>	59222.34	−212.88	0.52	19.32	0.24	0.25
<i>c</i>	59301.24	−212.88	0.08	17.85	0.14	−0.20
<i>c</i>	59302.25	−212.83	0.13	17.67	0.10	−0.97
<i>c</i>	59307.23	−212.88	0.16	17.55	0.23	−0.91
<i>c</i>	59363.10	−212.58	0.15	16.27	0.15	−0.69
<i>c</i>	59365.03	−212.32	0.13	16.15	0.11	−0.21
<i>c</i>	59631.28	−211.75	0.53	10.04	0.37	−0.85

Notes. ⁰ A correlation coefficient (ρ) is necessary to describe the alignment of the uncertainties of these interferometric observations with the on-sky coordinates. The covariance matrix can be reconstructed with $\sigma_{\Delta R.A.}^2$ and $\sigma_{\Delta Decl.}^2$ on the diagonal, and $\rho\sigma_{\Delta R.A.}\sigma_{\Delta Decl.}$ on the off-diagonal.

of mass, match those from Wang et al. (2020) and Wang et al. (2021) and are designed to be uninformative. Given that the 95% confidence interval (CI) on the planetary masses from Wang et al. (2021) covers the majority of their 1 – 15 M_{Jup} mass uniform prior, we extend the upper edge of this prior to 30 M_{Jup} . We also set the lower end of the prior to zero, since planets less massive than 1 M_{Jup} can still open gaps in protoplanetary disks (Rosotti et al. 2016). We set a Gaussian prior for parallax based on the system parallax of 8.8975 ± 0.0191 mas from Gaia DR3 (Gaia Collaboration et al. 2021). We also used the same Gaussian prior for the stellar mass as Wang et al. (2021), with a mean of 0.88 M_{\odot} and a standard deviation of 0.09 M_{\odot} , based on their stellar SED fit with 10% errors to account for systematics of their model.

3.1.1. Coplanarity vs Stability

In order to constrain the orbital parameter space for the system, we produced two orbital fits, one assuming stability of the orbits and the other assuming coplanarity between the orbits and the protoplanetary disk. In the case where we assumed stability, we imposed the prior given by Equation(1) of Wang et al. (2020), ensuring the non-crossing of the orbits of *b* and *c*:

$$a_c(1 - e_c) > a_b(1 + e_b). \quad (1)$$

In the scenario assuming coplanarity we placed a constraint on the mutual inclination between the two planets, as well as each planet and the PDS 70 protoplanetary disc. The mutual inclination Φ_{12} between two orbital planes (with inclinations i_1 and i_2 and longitudes of the ascending node Ω_1 and Ω_2) is given by the law of cosines (e.g., Bean & Seifahrt 2009):

$$\cos(\Phi_{12}) = \cos(i_1)\cos(i_2) + \sin(i_1)\sin(i_2)\cos(\Omega_1 - \Omega_2). \quad (2)$$

Figure 1 shows sample orbits taken from the posterior of the coplanar fit, plotted alongside the astrometry used for the fit.

We set the inclination and position angle (PA) of the disk to $i = 128.3$ degrees (equivalent to $i = 51.7$ degrees but for clockwise orbits) and $PA = 156.7$ degrees based on the values from Keppler et al. (2019). In the coplanar scenario, we placed Gaussian priors on all three of the mutual inclinations between *b*, *c*, and the protoplanetary disc, with a mean of 0 degrees and a standard deviation of 10 degrees, matching the prior on the coplanar model used in Wang et al. (2020).

In order to reduce convergence time, for both the stable and coplanar scenarios, we set the initial positions of the MCMC walkers using random draws from a Gaussian centred at the respective median parameters found by Wang et al. (2021) and with standard deviations matching the size of the largest 68% CI for each parameter.

For both the stable and coplanar fits, the median of the posterior for each parameter, as well as the 68% and 95% CIs on either side are shown in Table 3. The full posteriors for the orbital parameters of *b* and *c* are shown in Appendix C in Figures C.1 and C.2 respectively. In all cases the inclination of the disk falls within the 95% CIs for both *b* and *c*, indicating that both planets are coplanar with the disk.

Table 3. Orbital parameters fit to astrometry of PDS 70 *b* and *c* only. The third column shows the results of the fit using the Gaussian prior on the mutual inclination (see Equation 2), while the final two columns show the results of the fit using Equation 1 as a prior, before and after the *N*-body analysis. For each parameter the median value of the posterior is listed, with subscripts and superscripts listing the 68% and 95% CIs (with the 95% CIs in parentheses).

Quantity	Prior	Coplanar	Stable	Stable (incl. <i>N</i> -body)
a_b (au)	LogUniform(1, 100)	20.1 ^{+0.7(+1.5)} _{-0.7(-1.4)}	20.8 ^{+0.6(+1.3)} _{-0.7(-1.4)}	20.7 ^{+0.6(+1.4)} _{-0.5(-1.2)}
e_b	Uniform(0, 1)	0.21 ^{+0.05(+0.10)} _{-0.05(-0.10)}	0.18 ^{+0.05(+0.12)} _{-0.05(-0.09)}	0.16 ^{+0.05(+0.12)} _{-0.04(-0.01)}
i_b (deg)	$\sin(i)$	130.7 ^{+1.9(+3.8)} _{-1.9(-3.7)}	130.3 ^{+1.8(+3.9)} _{-1.8(-3.4)}	130.6 ^{+1.6(+3.5)} _{-1.6(-3.2)}
ω_b (deg)	Uniform(0, 360)	197 ⁺⁸⁽⁺¹⁴⁾ ₋₈₍₋₁₉₎	193 ⁺⁹⁽⁺¹⁶⁾ ₋₁₀₍₋₂₂₎	190 ⁺¹⁰⁽⁺¹⁶⁾ ₋₁₃₍₋₂₈₎
Ω_b (deg)	Uniform(0, 360)	178.2 ^{+4.5(+9.1)} _{-4.1(-8.0)}	179 ⁺⁵⁽⁺¹¹⁾ ₋₄₍₋₈₎	176 ⁺⁵⁽⁺¹²⁾ ₋₄₍₋₈₎
τ_b	Uniform(0, 1)	0.373 ^{+0.024(+0.047)} _{-0.021(-0.040)}	0.360 ^{+0.027(+0.051)} _{-0.023(-0.045)}	0.355 ^{+0.028(+0.055)} _{-0.025(-0.049)}
a_c (au)	LogUniform(1, 100)	31.9 ^{+0.9(+1.8)} _{-1.0(-2.0)}	33.3 ^{+1.1(+2.0)} _{-1.0(-2.2)}	33.9 ^{+1.0(+1.7)} _{-1.1(-2.1)}
e_c	Uniform(0, 1)	0.065 ^{+0.017(+0.036)} _{-0.015(-0.029)}	0.046 ^{+0.014(+0.032)} _{-0.013(-0.027)}	0.042 ^{+0.014(+0.027)} _{-0.013(-0.030)}
i_c (deg)	$\sin(i)$	131.5 ^{+1.2(+2.5)} _{-1.1(-2.2)}	130.4 ^{+1.3(+2.8)} _{-1.2(-2.2)}	129.8 ^{+1.3(+2.7)} _{-1.0(-1.9)}
ω_c (deg)	Uniform(0, 360)	89 ⁺⁹⁽⁺²¹⁾ ₋₁₀₍₋₂₄₎	77 ⁺¹¹⁽⁺³³⁾ ₋₁₁₍₋₂₂₎	77 ⁺¹²⁽⁺²⁸⁾ ₋₁₃₍₋₂₅₎
Ω_c (deg)	Uniform(0, 360)	154.9 ^{+2.1(+4.0)} _{-2.6(-5.8)}	157.5 ^{+1.8(+3.3)} _{-2.2(-5.8)}	158.0 ^{+1.7(+3.1)} _{-2.0(-3.8)}
τ_c	Uniform(0, 1)	0.572 ^{+0.030(+0.068)} _{-0.035(-0.078)}	0.52 ^{+0.04(+0.11)} _{-0.03(-0.07)}	0.521 ^{+0.038(+0.085)} _{-0.038(-0.070)}
Parallax (mas)	$\mathcal{N}(8.8975, 0.0191)$	8.880 ^{+0.024(+0.048)} _{-0.024(-0.051)}	8.881 ^{+0.025(+0.048)} _{-0.023(-0.046)}	8.878 ^{+0.026(+0.050)} _{-0.023(-0.046)}
M_b (M_{Jup})	Uniform(0, 30)	10 ⁺¹⁰⁽⁺¹⁸⁾ ₋₇₍₋₁₀₎	6 ⁺⁶⁽⁺¹⁸⁾ ₋₄₍₋₆₎	1.4 ^{+2.1(+4.2)} _{-1.0(-1.3)}
M_c (M_{Jup})	Uniform(0, 30)	9 ⁺⁸⁽⁺¹⁸⁾ ₋₆₍₋₉₎	9 ⁺⁹⁽⁺¹⁹⁾ ₋₆₍₋₈₎	6.4 ^{+4.3(+8.8)} _{-3.7(-5.7)}
M_* (M_{\odot})	$\mathcal{N}(0.88, 0.09)$	0.967 ^{+0.033(+0.067)} _{-0.030(-0.060)}	0.954 ^{+0.032(+0.070)} _{-0.031(-0.063)}	0.952 ^{+0.032(+0.065)} _{-0.028(-0.063)}

3.1.2. *N*-body Stability Analysis

While the fulfillment of Equation 1 is necessary for the stability of the PDS 70 planets, it does not ensure long-term stability. Therefore we performed an additional step of *N*-body stability analysis on the parameter sets resulting from the MCMC fit where this prior was used. We used the REBOUND *N*-body package (Rein & Liu 2012) with IAS15, a 15th order Gauss–Radau integrator (Rein & Spiegel 2015), to evolve these parameter sets backwards by 2.0 Myr. Parameter sets were deemed to be unstable if

- a) the planets passed within one Hill radius (~ 3.3 au) of each other or
- b) any of the planets were ejected to more than 40 au from their host star.

We chose 40 au as the ejection radius since it is the location of the outer edge of the dust gap in the PDS 70 system.

We chose a timescale of 2.0 Myr to match the lower bound of the type II migration timescale for the PDS 70 planets. The migration timescale is the time required for a planet to migrate inwards all the way to its host star due to gas drag from the circumstellar disk (Ida et al. 2018). A planet still embedded in a gas disk undergoes type I migration (Tanaka et al. 2002), whose timescale (neglecting contributions other than the Lindblad torque) is given by

$$t_{\text{mig1}} \simeq \frac{1}{2c} \left(\frac{M_p}{M_*} \right)^{-1} \left(\frac{\Sigma r^2}{M_*} \right)^{-1} \left(\frac{H}{r} \right)^2 \Omega^{-1}, \quad (3)$$

where $c \sim 2$ (Kanagawa et al. 2018) is a constant, M_p is the planet mass, Σ is the surface density of the circumstellar disk, r is the distance from the star, H is the gas scale height of the disk and Ω is the Keplerian frequency. A planet inside a disk

gap undergoes type II migration (Kanagawa et al. 2018), whose timescale is given by

$$t_{\text{mig2}} \simeq \frac{\Sigma}{\Sigma_{\text{min}}} t_{\text{mig1}}, \quad (4)$$

where Σ_{min} is the gas surface density in the gap. We used the radial parameterizations of Σ and h , as well as Σ_{min} , from Portilla-Revelo et al. (2023) to determine that $t_{\text{mig2}} \gtrsim 2.0$ Myr for the PDS 70 planets.

Of the 10 million available parameter sets from the results of the MCMC fit assuming non-crossing orbits ~ 8.9 million were determined to be unstable as a result of the *N*-body stability analysis. The final column of Table 3 shows the median for each parameter after this stability analysis, as well as the 68% and 95% CIs on each side.

Figure 2 shows the posterior distributions of the planetary masses, for the fit assuming stability, before and after performing *N*-body stability analysis. Using these parameter sets, we derived 95% confidence upper mass limits of $4.9 M_{\text{Jup}}$ for PDS 70 *b* and $13.6 M_{\text{Jup}}$ for PDS 70 *c*. These mass limits are defined such that only the highest 5% of the mass posterior lies above them. Without the *N*-body analysis, the posteriors of both the coplanar and stable fits are not informative enough to constrain the planet masses, since the 95% CIs cover most of the prior.

3.2. Two Planets or Three?

Christiaens et al. (2024) suggest the existence of a third proto-planet candidate, PDS 70 *d* in the PDS 70 system, from the detection of a point-like signal near the outer edge of the inner disk. While this signal is consistent with similar features observed by Mesa et al. (2019) and Hammond et al. (2025), we cannot eliminate the possibility that it belongs to a disk feature. In this section

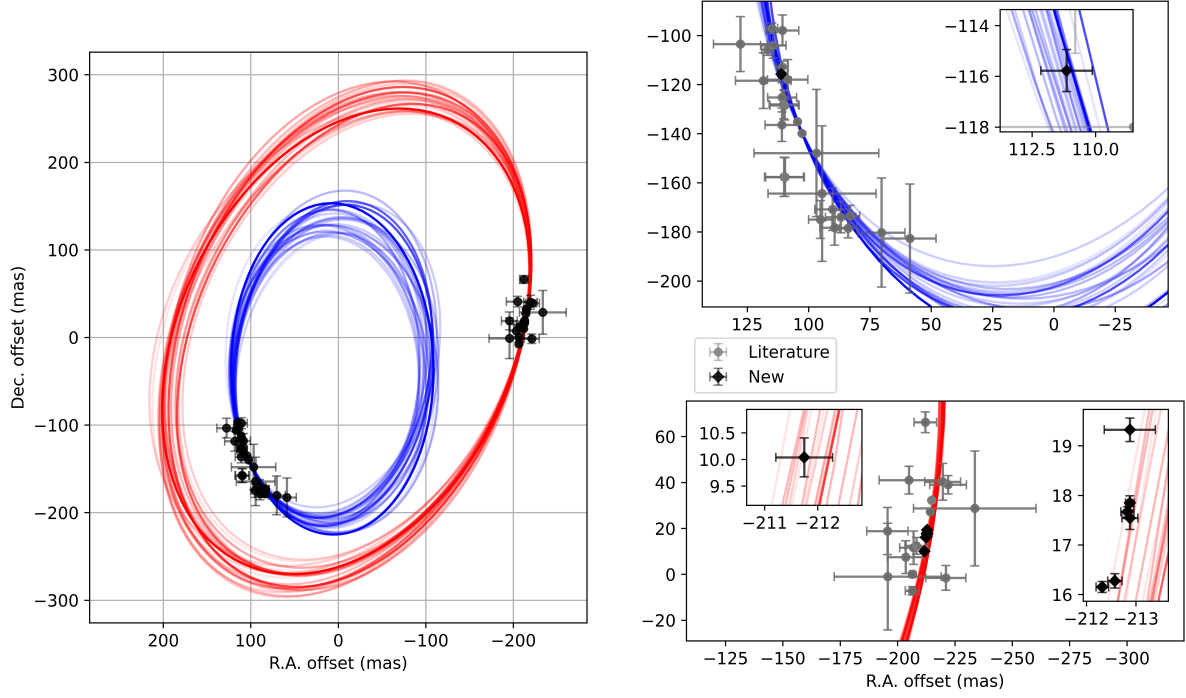


Fig. 1. Sample orbits from the posterior of the coplanar fit to PDS 70 *b* and *c* only, plotted alongside the astrometry used in the fit. Sample orbits for *b* are shown in blue, while sample orbits for *c* are shown in red. Zoomed in portions of the orbit, containing all the astrometry used in the fit, are shown in the right hand panels. The new GRAVITY astrometry (see Table 2) is shown in black and literature astrometry is shown in gray. The inset panels zoom-in on the new astrometry. R.A. and Dec. are given relative to the central star

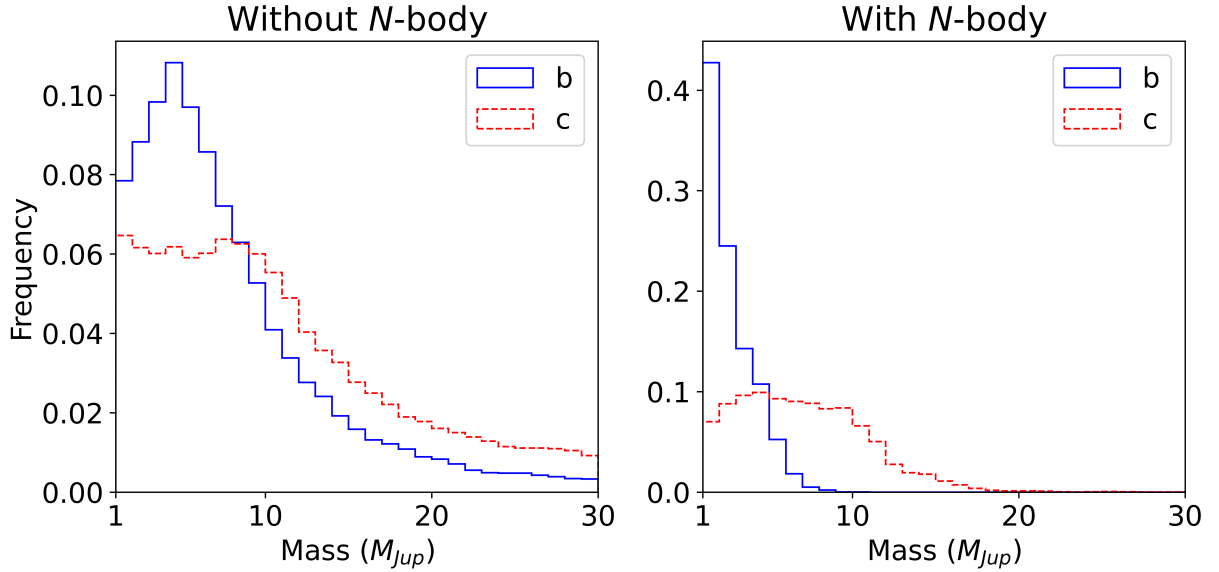


Fig. 2. Posterior distributions of the planet masses from the stable fit to PDS 70 *b* and *c* only, before and after *N*-body stability analysis. The mass posteriors for *b* are shown in blue (solid line), while the posteriors for *c* are shown in red (dashed line).

we fit orbits to *b*, *c* and the candidate *d* to assess possible orbital configurations and their stability.

We used the same orbital fitting procedure and MCMC settings as described in Section 3.1 to fit orbits to a three planet system described by astrometry of PDS 70 *b*, *c* and the candidate *d*. In addition to the astrometry described in Section 3.1, we used

astrometry from Christiaens et al. (2024) and Hammond et al. (2025) to fit the orbit of *d* (listed in Table B.1 in Appendix B).

In addition to the orbital parameters described in Section 3.1, we also fit a , e , i , ω , Ω , τ and M to *d*, with priors matching those for *b* and *c*. In the case of the parameters shared with the two-planet model, we set the initial positions of the MCMC walkers as described in Section 3.1. In the case of the parameters spe-

cific to PDS 70 d , we set the initial positions of the walkers by fitting these parameters to the PDS 70 d astrometry alone using orbitize!, with the same MCMC setting as described in Section 3.1. The positions of the walkers for the fit to b , c and the candidate d were set using random draws from a Gaussian centered at the median values found by this fit, with a standard deviation equivalent to the size of the largest 68% CI for each parameter.

We produced two orbital fits using this astrometry, one assuming coplanarity and one assuming stability, with conditions identical to those described in Section 3.1.1. The same type of N -body stability analysis as described in Section 3.1.2 was applied to the fit assuming stability, in order to further constrain the parameters. Out of the 10 million available parameter sets from the MCMC orbital fit, only ~ 6000 were determined to be stable orbital configurations.

Table 4 shows the median values of each parameter, as well as the 68% and 95% CIs, for both the coplanar and stable fits. Full posteriors for the orbital parameters of b , c and the candidate d are shown in Appendix C in Figures C.3, C.4 and C.5 respectively. Sample orbits taken from both the coplanar and stable fits are shown in Figure 3.

In all cases the inclination of the disk falls within the 95% CIs for the inclination of b and c , again indicating that these planets are coplanar with the disk. This is also true for the candidate d in the coplanar case, however both the stable and N -body case suggest somewhat higher inclinations for d .

In this scenario the N -body stability analysis allows us to place new 95% confidence upper mass limits for b and c . For b we find an upper mass limit of $5.3 M_{\text{Jup}}$, while for c we find an upper mass limit of $7.5 M_{\text{Jup}}$. In addition, for d we find a 95% confidence upper mass limit of $2.2 M_{\text{Jup}}$. Figure 4 shows the posterior distributions of the planetary masses both before and after performing N -body stability analysis.

3.3. Period Ratios

Wang et al. (2021) give the period ratio of c to b as $2.13^{+0.27}_{-0.24}$ for the 68% CI and $2.13^{+0.56}_{-0.45}$ for the 95% CI, putting them near the 2:1 mean-motion resonance (MMR) and excluding to a few σ other first-order MMRs such as 3:2 and 4:3. Table 5 lists the period ratios between each pair of planets that we found in our fits. Our fits to b and c only also find that the 2:1 MMR is the best candidate for the orbital resonance of these planets.

For our fits to b , c and the candidate d , the period ratios between b and c are all consistent with a 2:1 MMR, excluding the 3:2 and 4:3 MMRs. However, while in the coplanar case the period ratio between b and the candidate d is consistent with a 2:1 MMR the stable and N -body cases are more consistent with a 3:1 MMR. The coplanar case is also consistent with a 3:2 MMR within 2σ .

4. Comparison to Evolutionary Models

We used luminosity data from the Spiegel & Burrows (2012) evolutionary models to differentiate between hot-, warm-, and cold-start scenarios for the PDS 70 planets. These models give the flux density at $d = 10$ pc, from 0.8 to $15.0 \mu\text{m}$, for planets of mass $M_p = 1\text{--}15 M_{\text{Jup}}$ for initial, i.e., post-formation, entropies $S_i = 8\text{--}13 k_B/\text{baryon}$, for ages of $t = 1\text{--}1000$ Myr. To obtain the bolometric luminosity of each model, we integrated the flux and multiplied by $4\pi d^2$ to convert from flux to luminosity.

Entropy is defined physically only up to an additive constant. Naturally, we use the entropy zero-point adopted by Spiegel & Burrows (2012), who used the version of the Saumon et al. (1995) equation of state that is offset by $\Delta S = 0.52 k_B/\text{baryon}$ compared to the published tables (see Marleau & Cumming 2014 and Footnote 2 of Mordasini et al. 2017). This applies also to the values in Burrows et al. (1997), Marley et al. (2007), Mollière & Mordasini (2012), or Mordasini et al. (2017), while the MESA code (e.g., Paxton et al. 2011; Jermyn et al. 2023), Berardo et al. (2017), or Marleau & Cumming (2014) use the published Saumon et al. (1995) tables. The upshot of the offset is that, at a given mass, a Spiegel & Burrows (2012) model with (current) entropy S will have the same luminosity as a MESA model of entropy $S + \Delta S$.

Figures 5 and 6 show example mass–luminosity curves at the PDS 70 system age of 5.4 ± 1.0 Myr (i.e., isochrones) for different values of S_i , from the Spiegel & Burrows (2012) model. We calculated the luminosity at each mass value by linearly interpolating the age–luminosity relation for that mass at the system age. The shaded areas around the curves show the possible luminosity values given the uncertainty on the age of the system.

The blue boxes on the left panels of Figures 5 and 6 show the range of possible masses and luminosities for PDS 70 b given the 95% confidence upper mass limits from the 2-planet (Section 3.1) and 3-planet (Section 3.2) orbital parameter fits respectively. Similarly, the red boxes on the left panels of Figures 5 and 6 show the range of possible masses and luminosities for PDS 70 c given the upper mass limit from each fit. Luminosities are taken from Tables 3 and 4 of Wang et al. (2020). Since these tables each contain four different sets of luminosity bounds (from four different spectral energy distribution models), the lowest and the highest bounds of the four are used as the low and high bounds for the planet luminosity in this paper.

From the left-hand panels of Figures 5 and 6 it is apparent that the coldest post-formation entropies are inconsistent with the observed luminosities of PDS 70 b and c given the mass constraints from both the two-planet and three-planet fits.

We used the upper mass limits for these planets, determined in Section 3, to calculate the minimum values of S_i necessary for their formation. The right-hand panels of Figures 5 and 6 show the luminosity– S_i relation for each planet at their upper mass limit. Since luminosity monotonically increases with S_i , the minimum value of S_i for the planet occurs where luminosity hits the lower bound for the planet. The luminosity– S_i relation is given assuming the lower bound of 4.4 Myr for the system age, since this is where the model is brightest within the age range for PDS 70.

For PDS 70 b we calculated a lower limit for S_i of 9.9 k_B/baryon using the upper mass limit from the two-planet fit and 9.8 k_B/baryon using the upper mass limit from the three-planet fit. For PDS 70 c we calculated a lower limit of 8.5 k_B/baryon using the upper mass limit from the two-planet fit and 8.7 k_B/baryon using the upper mass limit from the three-planet fit.

5. Discussion

5.1. The Nature of PDS 70 d

From the currently available data the nature of PDS 70 d is unclear. It is located close to the outer edge of the inner disk and has been consistently detected with multiple telescopes and instruments over multiple epochs (Mesa et al. 2019; Christiaens et al. 2024; Hammond et al. 2025). However, its spectrum is

Table 4. Same as Table 3, but with orbital parameters fit to astrometry of PDS 70 *b*, *c* and the candidate *d*.

Quantity	Prior	Coplanar	Stable	Stable (incl. <i>N</i> -body)
a_b (au)	LogUniform(1, 100)	$19.8^{+0.6(+1.1)}_{-0.6(-1.1)}$	$20.6^{+0.5(+1.1)}_{-0.5(-1.1)}$	$21.1^{+0.4(+0.6)}_{-0.8(-1.0)}$
e_b	Uniform(0, 1)	$0.207^{+0.041(+0.085)}_{-0.041(-0.080)}$	$0.183^{+0.05(+0.09)}_{-0.04(-0.09)}$	$0.131^{+0.035(+0.069)}_{-0.037(-0.048)}$
i_b (deg)	$\sin(i)$	$131.7^{+1.9(+3.9)}_{-1.8(-3.4)}$	$130.8^{+1.7(+3.5)}_{-1.7(-3.4)}$	$128.7^{+1.9(+3.4)}_{-1.2(-3.7)}$
ω_b (deg)	Uniform(0, 360)	$191^{+6(+16)}_{-5(-10)}$	$194^{+5(+11)}_{-6(-15)}$	$191.4^{+2.7(+4.9)}_{-3.6(-5.1)}$
Ω_b (deg)	Uniform(0, 360)	$175.7^{+4.4(+9.6)}_{-3.3(-6.1)}$	$177.9^{+4.4(+9.2)}_{-3.7(-7.6)}$	$174.3^{+3.4(+8.1)}_{-2.9(-3.8)}$
τ_b	Uniform(0, 1)	$0.366^{+0.021(+0.041)}_{-0.018(-0.034)}$	$0.365^{+0.022(+0.043)}_{-0.017(-0.034)}$	$0.387^{+0.008(+0.010)}_{-0.024(-0.039)}$
a_c (au)	LogUniform(1, 100)	$32.5^{+0.9(+1.8)}_{-0.9(-1.9)}$	$34.6^{+0.9(+1.6)}_{-1.0(-2.3)}$	$35.3^{+0.8(+1.0)}_{-0.9(-2.2)}$
e_c	Uniform(0, 1)	$0.062^{+0.019(+0.039)}_{-0.014(-0.028)}$	$0.036^{+0.014(+0.028)}_{-0.010(-0.021)}$	$0.033^{+0.011(+0.016)}_{-0.008(-0.017)}$
i_c (deg)	$\sin(i)$	$130.5^{+1.2(+2.8)}_{-1.1(-2.0)}$	$129.1^{+1.2(+2.8)}_{-1.0(-1.8)}$	$128.5^{+1.4(+2.9)}_{-0.7(-0.8)}$
ω_c (deg)	Uniform(0, 360)	$94^{+8(+14)}_{-18(-30)}$	$66^{+12(+38)}_{-10(-21)}$	$63^{+19(+23)}_{-13(-21)}$
Ω_c (deg)	Uniform(0, 360)	$155.3^{+2.0(+3.6)}_{-2.3(-5.0)}$	$158.8^{+1.6(+3.3)}_{-2.3(-6.0)}$	$159.8^{+1.0(+2.2)}_{-0.8(-2.9)}$
τ_c	Uniform(0, 1)	$0.585^{+0.026(+0.047)}_{-0.055(-0.097)}$	$0.49^{+0.04(+0.13)}_{-0.03(-0.06)}$	$0.482^{+0.049(+0.063)}_{-0.051(-0.066)}$
a_d (au)	LogUniform(1, 100)	$12.9^{+1.6(+3.5)}_{-1.6(-2.9)}$	$10.7^{+1.5(+2.6)}_{-1.3(-2.3)}$	$10.7^{+2.1(+2.2)}_{-1.1(-2.3)}$
e_d	Uniform(0, 1)	$0.21^{+0.12(+0.24)}_{-0.10(-0.18)}$	$0.27^{+0.15(+0.29)}_{-0.15(-0.25)}$	$0.25^{+0.13(+0.30)}_{-0.23(-0.25)}$
i_d (deg)	$\sin(i)$	$136^{+5(+11)}_{-5(-10)}$	$153^{+13(+22)}_{-12(-21)}$	$151^{+6(+18)}_{-8(-23)}$
ω_d (deg)	Uniform(0, 360)	$80^{+150(+220)}_{-30(-60)}$	$80^{+110(+220)}_{-60(-80)}$	$29^{+24(+51)}_{-17(-26)}$
Ω_d (deg)	Uniform(0, 360)	$161^{+12(+25)}_{-18(-37)}$	$190^{+130(+160)}_{-50(-130)}$	$144^{+21(+38)}_{-10(-22)}$
τ_d	Uniform(0, 1)	$0.58^{+0.12(+0.21)}_{-0.40(-0.54)}$	$0.47^{+0.09(+0.18)}_{-0.09(-0.20)}$	$0.55^{+0.04(+0.09)}_{-0.08(-0.15)}$
Parallax (mas)	$\mathcal{N}(8.8975, 0.0191)$	$8.872^{+0.025(+0.048)}_{-0.031(-0.058)}$	$8.881^{+0.024(+0.045)}_{-0.025(-0.058)}$	$8.882^{+0.018(+0.059)}_{-0.021(-0.025)}$
M_b (M_{Jup})	Uniform(0, 30)	$10^{+9(+18)}_{-5(-9)}$	$5^{+4(+11)}_{-3(-4)}$	$0.7^{+1.7(+4.6)}_{-0.5(-0.7)}$
M_c (M_{Jup})	Uniform(0, 30)	$9^{+7(+18)}_{-5(-8)}$	$8^{+8(+18)}_{-5(-7)}$	$2.4^{+4.3(+5.8)}_{-1.3(-2.2)}$
M_d (M_{Jup})	Uniform(0, 30)	$8^{+7(+16)}_{-6(-8)}$	$9^{+9(+18)}_{-7(-9)}$	$0.4^{+1.5(+1.9)}_{-0.3(-0.4)}$
M_* (M_\odot)	$\mathcal{N}(0.88, 0.09)$	$0.960^{+0.032(+0.065)}_{-0.031(-0.063)}$	$0.953^{+0.031(+0.062)}_{-0.033(-0.064)}$	$0.965^{+0.041(+0.068)}_{-0.025(-0.088)}$

Table 5. Period ratios between the PDS 70 planets. The period ratios from the fits using only astrometry from PDS 70 *b* and *c* are shown in the first row. The remaining rows show the period ratios between each pair of planets from the fits where astrometry from *b*, *c* and the candidate *d* is used. For each fit the median value of the posterior is shown, with subscripts and superscripts listing the 68% and 95% CIs (with the 95% CIs in parentheses).

Period Ratio	Astrometry	Coplanar	Stable	Stable (incl. <i>N</i> -body)
$c:b$	b, c	$1.99^{+0.15(+0.29)}_{-0.13(-0.26)}$	$2.02^{+0.15(+0.29)}_{-0.13(-0.25)}$	$2.08^{+0.13(+0.22)}_{-0.12(-0.23)}$
$c:b$	b, c, d	$2.11^{+0.13(+0.28)}_{-0.13(-0.24)}$	$2.17^{+0.13(+0.26)}_{-0.12(-0.25)}$	$2.16^{+0.09(+0.21)}_{-0.05(-0.23)}$
$b:d$	b, c, d	$1.90^{+0.41(+0.91)}_{-0.32(-0.56)}$	$2.7^{+0.6(+1.2)}_{-0.5(-0.8)}$	$2.7^{+0.5(+1.3)}_{-0.6(-0.6)}$
$c:d$	b, c, d	$4.0^{+0.9(+1.9)}_{-0.7(-1.3)}$	$5.8^{+1.3(+2.6)}_{-1.0(-1.7)}$	$6.1^{+1.2(+2.3)}_{-1.5(-1.6)}$

more similar to star light reflected by dust than thermal emission by a planet (Mesa et al. 2019). This suggests two possibilities:

1. PDS 70 *d* is not a planet and is instead a disk feature, such as a dust clump
2. PDS 70 *d* is a planet embedded in a dust envelope

When *d* is included in the analysis the fraction of orbital configurations deemed to be stable after *N*-body analysis is small. The *N*-body analysis also indicates that *d* must have a comparatively low mass in order for the PDS 70 planetary system to remain stable. Either *N*-body analysis is very efficient at constraining the orbital parameter space for this system or there is a lack of stable orbit configuration for a three-body system. The latter case would suggest that *d* is a disk feature and not a planet.

It is important to note that we have not included the impacts of gas drag in our *N*-body analyses. While this is not important for PDS 70 *b* and *c*, since they sit comfortably inside the gap in the disk, the candidate *d* sits close to the outer edge of the inner disk. On short timescales planet-disk interaction dampens the eccentricity and inclination of the planet (Goldreich & Sari 2003; Tanaka & Ward 2004), which could therefore enhance the stability of the system.

5.2. Viability of Cold-Start Formation

Our analysis in Section 4 adds PDS 70 *b* and *c* to the list of directly-imaged exoplanets that are inconsistent with cold-

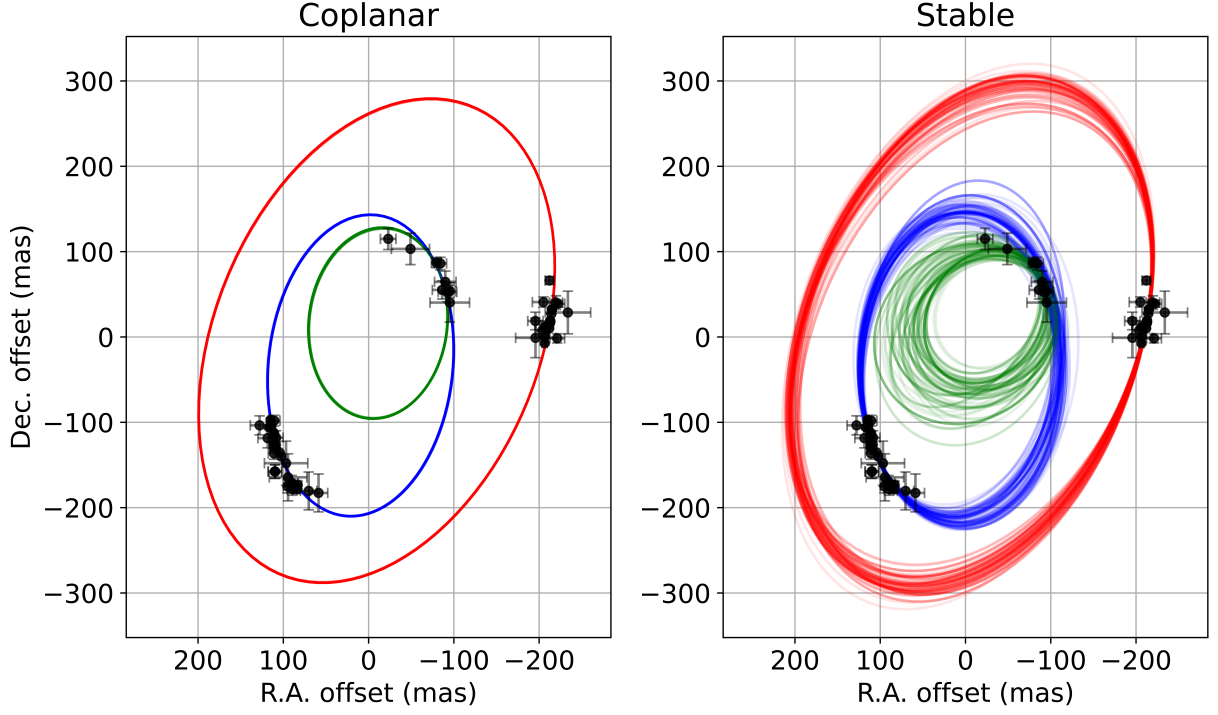


Fig. 3. Sample orbits from the fits to astrometry of PDS 70 *b*, *c* and the candidate *d*. The left panel shows orbits taken from the fit assuming coplanarity, while the right panel shows orbits taken from the fit assuming stability (before *N*-body analysis). Orbits for *b*, *c* and the candidate *d* are shown in blue, red and green respectively. The astrometry data is plotted with error bars in black. All astrometry is given relative to the central star. The coplanar fit produces many orbital configurations where the orbits of *b* and the candidate *d* overlap, even though these orbits would likely be unstable.

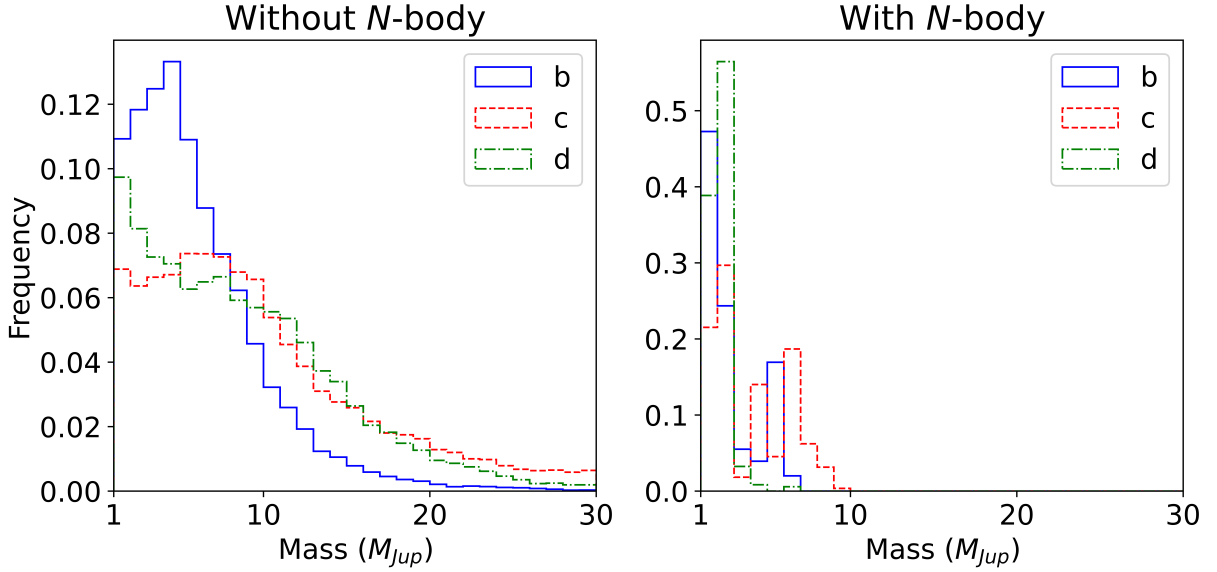


Fig. 4. Posterior distributions of the planet masses from the stable fit to PDS 70 *b*, *c* and the candidate *d*, before and after *N*-body stability analysis. The mass posteriors for *b* are shown in blue (solid line), the posteriors for *c* are shown in red (dashed line), and the posteriors for *d* are shown in green (line with dots and dashes). This analysis assumes that *d* is a planet and not a disk feature.

start formation. Marleau & Cumming (2014) found $S_i > 9.2$ k_B /baryon for 2M1207 b and the planets in the HR 8799 system, as well as $S_i > 10.5$ for β Pic b. Brandt et al. (2021a) used dynamical mass measurements of β Pic c to determine that it is inconsistent with the cold-start models of Spiegel & Burrows

(2012). While this may suggest that true cold-start giant planets are rare (or even non-existent), we cannot rule out observational bias. Given a constant mass and age, higher S_i leads to higher luminosity, and therefore these planets are more likely to be detected via direct-imaging surveys.

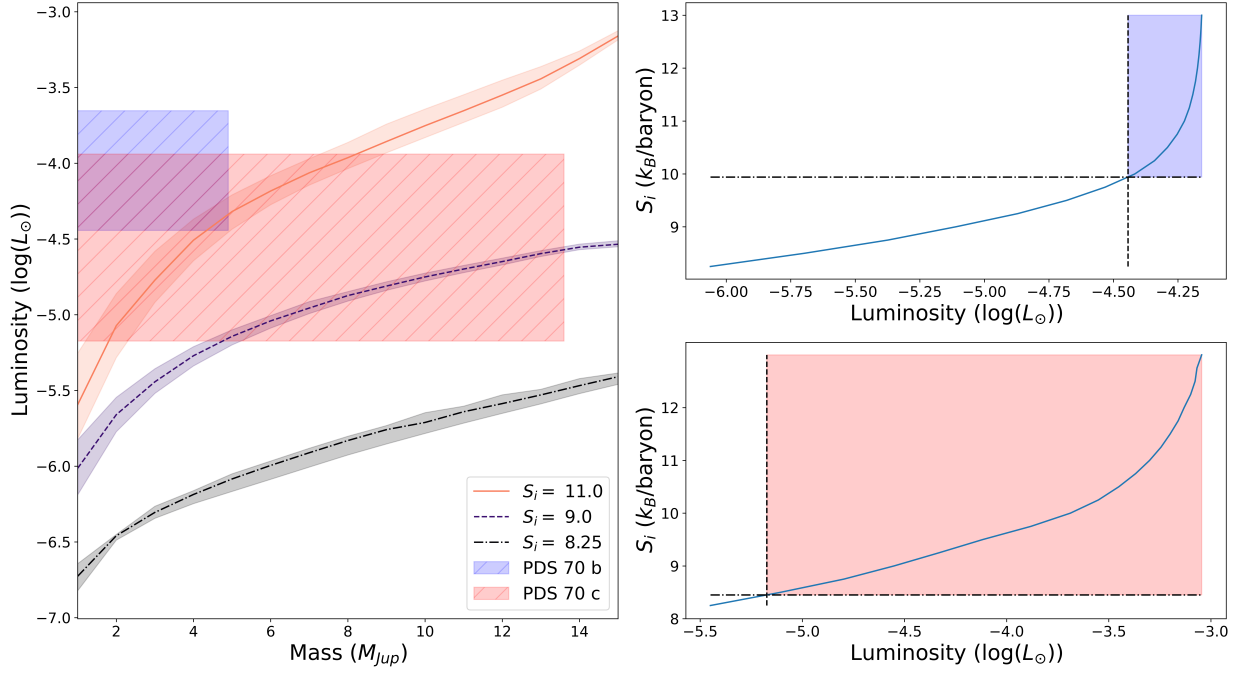


Fig. 5. Comparison of the upper mass limits for PDS 70 *b* and PDS 70 *c* from the two-planet orbital parameter fit to cold-, warm-, and hot-start evolutionary models from Spiegel & Burrows (2012). The mass-luminosity curves for the different models, taken at the PDS 70 system age of 5.4 Myr are shown in the left panel, with their corresponding post-formation entropies given in the legend. The ribbon around each curve corresponds to the uncertainty in age of PDS 70. The blue and red boxes in the left panel show the possible masses and luminosities for *b* and *c* respectively, with luminosities taken from Wang et al. (2020). The upper right panel shows the luminosity- S_i curve at the upper mass limit for *b*. The blue shaded area in this panel, bounded by the dashed and dashed-dotted lines shows the possible range of S_i for *b* from this orbital parameter fit. The lower right panel is the same as upper right panel, but for *c*.

5.3. Are the PDS 70 Planets Still Accreting?

In order to compare PDS 70 *b* and *c* to the Spiegel & Burrows (2012) evolutionary models, we have made the assumption that these planets are "done" accreting gas. Haffert et al. (2019) gives relatively low accretion rates of $\sim 0.01 M_{\text{Jup}} \text{ Myr}^{-1}$ for both planets, based on their H α emission. However, modelling of the spectral energy distribution of PDS 70 *c* by Choksi & Chiang (2025) suggests that its accretion rate could be as high as $0.6 M_{\text{Jup}} \text{ Myr}^{-1}$. This would result in the accretion of multiple M_{Jup} of gas before the dispersal of the protoplanetary disk, significantly increasing the luminosity of the planet and affecting the minimum S_i calculation.

Even if we assume that the accretion rates for these planets are low, our analysis in Section 4 also assumes that the planets are the same age as the star. If the planets formed more recently than the star, then their luminosity and mass will be consistent with lower S_i evolutionary tracks. To understand how this impacts our minimum S_i values, we performed the same analysis as in Section 4, but assuming a lower limit of 1 Myr on the age. For this analysis we used the mass limits given from the orbit fit to *b* and *c* only. In this case, we find a minimum S_i of $9.5 k_B/\text{baryon}$ for *b* and $8.4 k_B/\text{baryon}$ for *c*. Therefore, even if these planets are newly formed, they are still inconsistent with the coldest-start models.

Planet-planet collisions could also provide an additional source of heat, which is not accounted for in our determination of the minimum values of S_i . However, for giant planets of multiple Jupiter mass, planet-planet scattering tends to lead to planet ejection rather than collision (Rasio & Ford 1996; Weidenschilling & Marzari 1996).

6. Conclusions

Using new relative astrometry for PDS 70 *b* and *c* obtained with VLTI/GRAVITY we obtained updated orbital parameters for these planets, including dynamical mass estimates. Fitting to astrometry from *b* and *c* only, we calculated an upper mass limits (with 95% confidence) of $4.9 M_{\text{Jup}}$ for *b* and $13.6 M_{\text{Jup}}$ for *c*.

It is unclear whether PDS 70 *d* is a planet or a disk feature. Our *N*-body stability analysis of orbits fit to astrometry of *b*, *c* and the candidate *d* finds a relative lack of stable orbital configurations. However, we do not consider gas drag, which may lead to more stable orbits. From our orbital parameter fits that include *d*, we find 95% confidence upper mass limits of $5.3 M_{\text{Jup}}$, $7.5 M_{\text{Jup}}$, and $2.2 M_{\text{Jup}}$ for *b*, *c* and the candidate *d* respectively.

In all of our analyses the period ratio of PDS 70 *c* to *b* is consistent with a 2:1 MMR, while ruling out the 3:2 and 4:3 MMRs. When we include the candidate *d* and enforce coplanarity the period ratio of *b* to *d* is consistent with the 2:1 and 3:2 MMRs. However, when we enforce stability and when we employ *N*-body stability analysis the period ratio becomes inconsistent with both of these MMRs, and instead becomes more consistent with the 3:1 MMR.

We eliminate the possibility of a cold-start for both PDS 70 *b* and PDS 70 *c* through comparison of our dynamical mass estimates to hot-, warm- and cold-start evolutionary models. This is true of both the two-planet and three-planet fits. We determine a minimum S_i of $9.9 k_B/\text{baryon}$ for *b* using the two-planet fit, and of $9.8 k_B/\text{baryon}$ using the three-planet fit. Similarly, we determine a minimum S_i of $8.5 k_B/\text{baryon}$ for *c* using the two-planet fit and $8.7 k_B/\text{baryon}$ using the three-planet fit. Even in the case where these planets are newly-formed they are both inconsistent

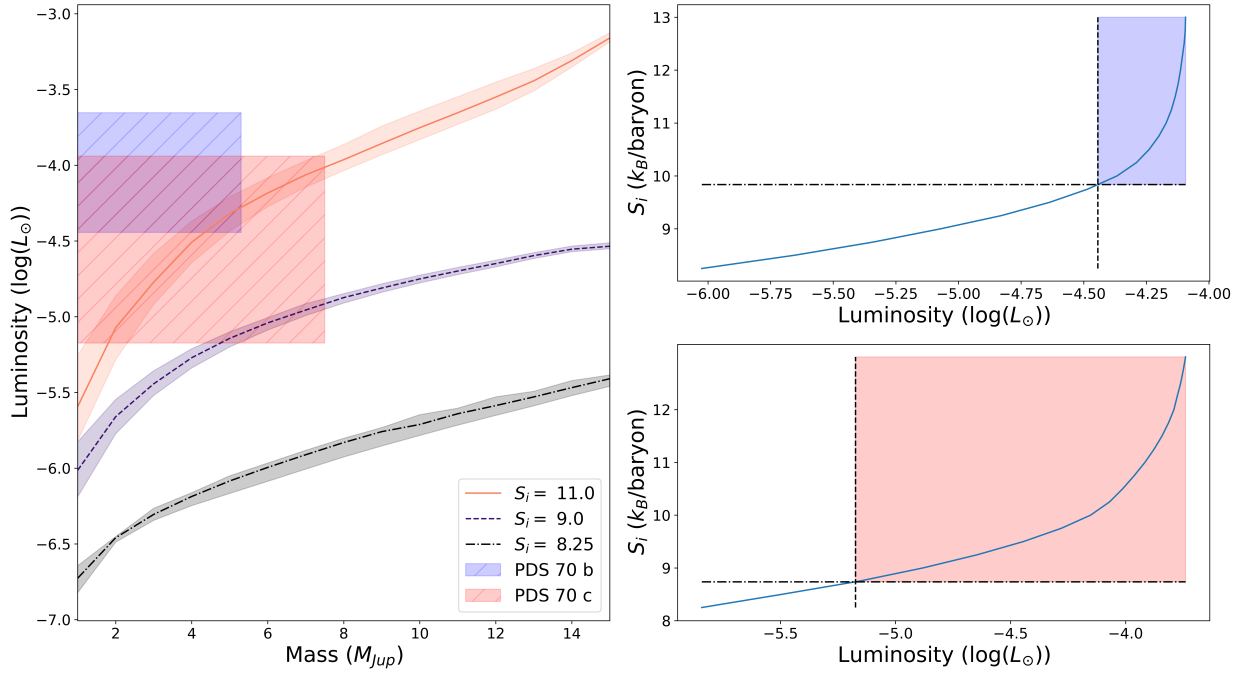


Fig. 6. Same as Figure 6, but with upper mass limits taken from the three-planet orbital parameter fit.

with the coldest-start models, with minimum S_i values of 9.5 k_B /baryon and 8.4 k_B /baryon respectively.

Acknowledgements. Based on observations collected at the European Organisation for Astronomical Research in the Southern Hemisphere under ESO programmes 1104.C-0651(A), 1104.C-0651(C) and 105.209D.001. We thank Zhoujian Zhang for useful discussions. I.H. acknowledges a Research Training Program scholarship from the Australian government. R.B. acknowledges the financial support from DFG under Germany’s Excellence Strategy EXC 2181/1-390900948, Exploratory project EP 8.4 (the Heidelberg STRUCTURES Excellence Cluster). J.S.-B. acknowledges the support received from the UNAM PAPIIT project IA 105023. G.-D.M. acknowledges the support from the European Research Council (ERC) under the Horizon 2020 Framework Program via the ERC Advanced Grant “ORIGINS” (PI: Henning), Nr. 832428, and via the research and innovation programme “PROTOPLANETS”, grant agreement Nr. 101002188 (PI: Benisty).

References

- Amara, A., & Quanz, S. P. 2012, *MNRAS*, **427**, 948
- Balmer, W. O., Franson, K., Chomez, A., et al. 2024, *arXiv e-prints*, [arXiv:2411.05917](#)
- Baraffe, I., Chabrier, G., Barman, T. S., Allard, F., & Hauschildt, P. H. 2003, *A&A*, **402**, 701
- Bean, J. L., & Seifahrt, A. 2009, *A&A*, **496**, 249
- Berardo, D., Cumming, A., & Marleau, G.-D. 2017, *ApJ*, **834**, 149
- Blakely, D., Johnstone, D., Cugno, G., et al. 2024, *arXiv e-prints*, [arXiv:2404.13032](#)
- Blunt, S., Wang, J. J., Angelo, I., et al. 2020, *AJ*, **159**, 89
- Bowler, B. P. 2016, *PASP*, **128**, 102001
- Brandt, G. M., Brandt, T. D., Dupuy, T. J., Li, Y., & Michalik, D. 2021a, *AJ*, **161**, 179
- Brandt, G. M., Brandt, T. D., Dupuy, T. J., Michalik, D., & Marleau, G.-D. 2021b, *ApJ*, **915**, L16
- Burrows, A., Marley, M., Hubbard, W. B., et al. 1997, *ApJ*, **491**, 856
- Choksi, N., & Chiang, E. 2025, *MNRAS*, **537**, 2945
- Christiaens, V., Casassus, S., Absil, O., et al. 2019, *MNRAS*, **486**, 5819
- Christiaens, V., Gonzalez, C., Farkas, R., et al. 2023, *The Journal of Open Source Software*, **8**, 4774
- Christiaens, V., Samland, M., Henning, T., et al. 2024, *A&A*, **685**, L1
- Close, L. M., Males, J. R., Li, J., et al. 2025, *AJ*, **169**, 35
- Foreman-Mackey, D., Hogg, D. W., Lang, D., & Goodman, J. 2013, *PASP*, **125**, 306
- Fortney, J. J., Marley, M. S., Saumon, D., & Lodders, K. 2008, *ApJ*, **683**, 1104
- Gaia Collaboration, Brown, A. G. A., Vallenari, A., et al. 2021, *A&A*, **649**, A1
- Goldreich, P., & Sari, R. 2003, *ApJ*, **585**, 1024
- Gomez Gonzalez, C. A., Wertz, O., Absil, O., et al. 2017, *AJ*, **154**, 7
- GRAVITY Collaboration, Abuter, R., Accardo, M., et al. 2017, *A&A*, **602**, A94
- GRAVITY Collaboration, Nowak, M., Lacour, S., et al. 2020, *A&A*, **633**, A110
- Haffert, S. Y., Bohn, A. J., de Boer, J., et al. 2019, *Nature Astronomy*, **3**, 749
- Hammond, I., Christiaens, V., Price, D. J., et al. 2025, *MNRAS*, TBD
- Ida, S., Tanaka, H., Johansen, A., Kanagawa, K. D., & Tanigawa, T. 2018, *ApJ*, **864**, 77
- Jermyn, A. S., Bauer, E. B., Schwab, J., et al. 2023, *ApJS*, **265**, 15
- Kanagawa, K. D., Tanaka, H., & Szuszkiewicz, E. 2018, *ApJ*, **861**, 140
- Keppler, M., Benisty, M., Müller, A., et al. 2018, *A&A*, **617**, A44
- Keppler, M., Teague, R., Bae, J., et al. 2019, *A&A*, **625**, A118
- Lapeyrère, V., Kervella, P., Lacour, S., et al. 2014, in *Society of Photo-Optical Instrumentation Engineers (SPIE) Conference Series*, Vol. 9146, Optical and Infrared Interferometry IV, ed. J. K. Rajagopal, M. J. Creech-Eakman, & F. Malbet, 91462D
- Linder, E. F., Mordasini, C., Mollière, P., et al. 2019, *A&A*, **623**, A85
- Marleau, G. D., & Cumming, A. 2014, *MNRAS*, **437**, 1378
- Marley, M. S., Fortney, J. J., Hubickyj, O., Bodenheimer, P., & Lissauer, J. J. 2007, *ApJ*, **655**, 541
- Marois, C., Lafrenière, D., Doyon, R., Macintosh, B., & Nadeau, D. 2006, *ApJ*, **641**, 556
- Mesa, D., Keppler, M., Cantalloube, F., et al. 2019, *A&A*, **632**, A25
- Mollière, P., & Mordasini, C. 2012, *A&A*, **547**, A105
- Mordasini, C., Marleau, G.-D., & Mollière, P. 2017, *A&A*, **608**, A72
- Müller, A., Keppler, M., Henning, T., et al. 2018, *A&A*, **617**, L2
- Nowak, M., Lacour, S., Lagrange, A. M., et al. 2020, *A&A*, **642**, L2
- Paxton, B., Bildsten, L., Dotter, A., et al. 2011, *ApJS*, **192**, 3
- Phillips, M. W., Tremblin, P., Baraffe, I., et al. 2020, *A&A*, **637**, A38
- Portilla-Revelo, B., Kamp, I., Facchini, S., et al. 2023, *A&A*, **677**, A76
- Rasio, F. A., & Ford, E. B. 1996, *Science*, **274**, 954
- Rein, H., & Liu, S. F. 2012, *A&A*, **537**, A128
- Rein, H., & Spiegel, D. S. 2015, *MNRAS*, **446**, 1424
- Riaud, P., Mawet, D., Absil, O., et al. 2006, *A&A*, **458**, 317
- Rosotti, G. P., Juhasz, A., Booth, R. A., & Clarke, C. J. 2016, *MNRAS*, **459**, 2790
- Saumon, D., Chabrier, G., & van Horn, H. M. 1995, *ApJS*, **99**, 713
- Saumon, R., Pueyo, L., & Larkin, J. 2012, *ApJ*, **755**, L28
- Sparks, W. B., & Ford, H. C. 2002, *ApJ*, **578**, 543
- Spiegel, D. S., & Burrows, A. 2012, *ApJ*, **745**, 174
- Tanaka, H., Takeuchi, T., & Ward, W. R. 2002, *ApJ*, **565**, 1257
- Tanaka, H., & Ward, W. R. 2004, *ApJ*, **602**, 388
- Vousden, W. D., Farr, W. M., & Mandel, I. 2016, *MNRAS*, **455**, 1919
- Wahhaj, Z., Benisty, M., Ginski, C., et al. 2024, *A&A*, **687**, A257
- Wang, J. J., Ginzburg, S., Ren, B., et al. 2020, *AJ*, **159**, 263
- Wang, J. J., Vigan, A., Lacour, S., et al. 2021, *AJ*, **161**, 148
- Weidenschilling, S. J., & Marzari, F. 1996, *Nature*, **384**, 619
- Zurlo, A., Goździewski, K., Lazzoni, C., et al. 2022, *A&A*, **666**, A133

Appendix A: New reduction of VLT/SINFONI data

Christiaens et al. (2019) reported the astrometry of planet *b* detected in VLT/SINFONI data acquired on 10 May 2014. For planet *c* the earliest reported astrometry is from a SPHERE dataset of 2018 (Mesa et al. 2019). Nonetheless the new reduction of the SINFONI dataset presented in Hammond et al. (2025) not only revealed candidate *d*, but also provided a clear detection of planet *c*. This paragraph summarizes how we calculated the astrometry for planet *c* from this dataset.

Details on the data calibration and processing can be found in Christiaens et al. (2019) and Hammond et al. (2025). For stellar PSF modeling and subtraction we considered principal component analysis (PCA; Soummer et al. 2012; Amara & Quanz 2012) to leverage in two consecutive steps both the spectral (SDI; Sparks & Ford 2002) and the angular differential imaging strategies (ADI; Marois et al. 2006). We used the 2-step PCA implementation in VIP (Gomez Gonzalez et al. 2017; Christiaens et al. 2023). We collapsed only the spectral channels longward of $2.3 \mu\text{m}$ during PCA-SDI, as these benefit from the highest Strehl ratio and the highest flux for planet *c*. For PCA-ADI, we considered a 1-FWHM rotation threshold at the separation of planet *c* when building the PCA library for each residual frame resulting from PCA-SDI.

Since the signals from planet *c* are merged with the signals from the illuminated edge of the outer disk, estimating its astrometry using classical point-source forward-modelling techniques would lead to biased estimates. Instead we first isolated the signal of *c* from the disk by subtracting a disk model. The disk model was built from the south side of the disk, leveraging the expected symmetry with respect to the semi-minor axis. In practice, we (i) rotated the image by an angle corresponding to $270^\circ - \text{PA}_\beta$, where PA_β is the semi-minor axis of the disk PA_β pointing to the near side of the disk, (ii) subtracted from each north or south half of the image the signals from the other half, and (iii) rotated back the image by $\text{PA}_\beta - 270^\circ$. A similar strategy as the direct negative fake companion technique presented in Christiaens et al. (2024) was then adopted to retrieve the astrometry of *c*.

The dominant source of uncertainty in this procedure is associated with the presence of faint residual extended signals similar to the spiral accretion stream reported in Christiaens et al. (2024), henceforth the figure of merit to be considered for optimal estimation of the astrometry of *c*. We therefore considered both a range of values for PA_β (252° to 260° per step of 0.5°), and two different figures of merit: (i) minimization of the absolute value of the determinant of the Hessian matrix at the estimated location of *c*, and (ii) minimization of the sum of absolute values of residual pixel intensities within an aperture at the estimated location of *c*. Two sub-cases were considered for (i) and (ii): a Hessian matrix of either 1×1 or 2×2 , and aperture sizes of 0.5 and 1 FWHM, respectively. This made for 68 estimates, which were visually vetted and considered plausible based on the shape of the outer disk edge after subtraction of *c*. The median value of these 68 astrometric estimates is reported in Table B.1. The subtraction of *c* with the optimal parameters found with this approach is shown in Figure A.1.

We considered the standard deviation of these 68 estimates as the uncertainty associated with the disk. As final uncertainties, we conservatively combined in quadrature (i) the uncertainty associated with the disk, (ii) the residual speckle noise uncertainties - assumed to be the same as reported for planet *b* in Christiaens et al. (2019), and (iii) systematic uncertainties on the plate scale and true north conservatively assumed to be 0.4 mas and

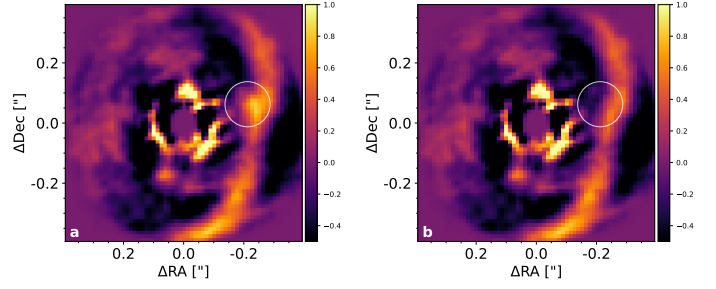


Fig. A.1. Final image obtained from our new reduction of the 2014-05-10 SINFONI data, before (a) and after (b) subtracting the estimated contribution of planet *c* as explained in Sec. A.

0.5° , respectively (Christiaens et al. 2019). These final uncertainties are also reported in Table B.1. We did not attempt to re-estimate the residual speckle noise uncertainty associated to *c*, due to the presence of bright and extended signals at that radius. Since the estimate for *b* was obtained after similar data processing, the latter can be considered as a conservative estimate of the residual speckle uncertainty, as *b* is slightly more inward than *c*.

Appendix B: Archival Data

Table B.1 collects the existing astrometry for both confirmed planets and for candidate *d* of the PDS 70 system.

Table B.1. Literature astrometry for PDS 70 *b*, *c* and *d*.

	Date	MJD (days)	Instrument	$\Delta R.A.$ (mas)	$\sigma_{\Delta R.A.}$ (mas)	$\Delta Dec.$ (mas)	$\sigma_{\Delta Decl.}$ (mas)	Sep. (mas)	$\sigma_{Sep.}$ (mas)	P.A. (deg)	$\sigma_{P.A.}$ (deg)	Ref.
<i>b</i>	2012-03-31	56017	NICI	58.7	10.7	-182.7	22.2	191.9	21.4	162.2	3.7	[1]
<i>b</i>	2014-05-10	56787	SINFONI	70.3	9.6	-180.3	5.9	193.5	4.9	158.7	3.0	[3]
<i>b</i>	2015-05-03	57145	IRDIS	83.1	3.9	-173.5	4.3	192.3	4.2	154.5	1.2	[1]
<i>b</i>	2015-05-03	57145	IRDIS	83.9	3.6	-178.5	4.0	197.2	3.9	154.9	1.1	[1]
<i>b</i>	2015-06-01	57174	IRDIS	89.4	6.0	-178.3	7.1	199.5	6.9	153.4	1.8	[1]
<i>b</i>	2015-06-01	57174	IRDIS	86.9	6.2	-174.0	6.4	194.5	6.3	153.5	1.8	[1]
<i>b</i>	2016-05-14	57522	IRDIS	90.2	7.3	-170.8	8.6	193.2	8.3	152.2	2.3	[1]
<i>b</i>	2016-05-14	57522	IRDIS	95.2	4.8	-175.0	7.7	199.2	7.1	151.5	1.6	[1]
<i>b</i>	2016-06-01	57540	NaCo	94.5	22.0	-164.4	27.6	189.6	26.3	150.6	7.1	[1]
<i>b</i>	2018-02-24	58174	IRDIS	109.6	7.9	-157.7	7.9	192.1	7.9	147.0	2.4	[2]
<i>b</i>	2018-02-24	58174	IRDIS	110.0	7.9	-157.6	8.0	192.2	8.0	146.8	2.4	[2]
<i>b</i>	2018-06-20	58289	MUSE	96.8	25.4	-147.9	25.9	176.8	25	146.8	8.5	[4]
<i>b</i>	2019-06-08	58642	NIRC2	110.9	6.8	-136.4	6.8	175.8	6.9	140.9	2.2	[6]
<i>b</i>	2019-07-16	58680	GRAVITY	102.626	0.087	-139.879	0.291	173.49	0.24	143.733	0.061	[7]
<i>b</i>	2020-02-10	58889	GRAVITY	104.545	0.229	-135.081	0.077	170.81	0.15	142.262	0.063	[7]
<i>b</i>	2021-07-15	59410	IRDIS	118	11	-118	11	167.5	11.0	135.0	4.0	[10]
<i>b</i>	2021-08-21	59447	IRDIS	108.5	8.2	-118.0	8.2	160.3	8.0	137.4	3.0	[10]
<i>b</i>	2021-08-22	59448	IRDIS	110.8	5.9	-125.2	5.9	167.2	6.0	138.5	2.0	[10]
<i>b</i>	2021-09-02	59459	IRDIS	109.8	5.9	-128.5	6.0	169.0	6.0	139.5	2.0	[10]
<i>b</i>	2021-09-04	59461	IRDIS	110.1	5.9	-128.0	6.0	168.9	6.0	139.3	2.0	[10]
<i>b</i>	2022-02-28	59638	IRDIS	114.3	5.2	-104.0	5.2	154.6	5.0	132.3	2.0	[10]
<i>b</i>	2022-04-24	59693	MagAO-X	110.8	2.3	-112.8	2.3	158.1	3.0	135.5	0.5	[11]
<i>b</i>	2023-02-24	59999	NIRISS	110.7	6.7	-97.9	6.3	147.8	8.2	131.5	1.6	[8]
<i>b</i>	2023-03-08	60011	MagAO-X	116.7	2.4	-105.8	2.3	157.5	3.0	132.18	0.5	[11]
<i>b</i>	2023-03-08	60011	NIRCam	128	11	-104	11	164.5	10.4	129.0	4.1	[9]
<i>b</i>	2024-03-25	60394	MagAO-X	115.0	2.4	-97.1	2.2	150.5	3.0	130.18	0.50	[11]
<i>c</i>	2014-05-10	56787	SINFONI	-212.1	10.5	66.2	7.3	222.2	10.3	287.3	2.0	[13]
<i>c</i>	2018-02-25	58174	IRDIS	-205.0	13.0	41.0	6.0	209	13	281.2	0.5	[5]
<i>c</i>	2018-06-20	58289	MUSE	-233.7	26.7	28.7	25.0	235.5	25.0	277.0	6.5	[4]
<i>c</i>	2019-03-06	58548	IRDIS	-222.0	8.0	39.0	4.0	225	8	279.9	0.5	[5]
<i>c</i>	2019-06-08	58642	NIRC2	-219.7	7.8	40.3	8.0	223.4	8.0	280.4	2.0	[6]
<i>c</i>	2019-07-19	58683	GRAVITY	-214.98	0.296	32.323	0.396	217.40	0.30	278.55	0.10	[7]
<i>c</i>	2019-07-19	58683	GRAVITY	-214.929	0.335	32.222	0.437	217.33	0.34	278.53	0.11	[7]
<i>c</i>	2020-02-10	58889	GRAVITY	-214.333	0.144	27.212	0.249	216.05	0.15	277.236	0.066	[7]
<i>c</i>	2021-07-15	59410	IRDIS	-208.2	5.0	12.4	3.6	208.6	5.0	273.4	1.0	[10]
<i>c</i>	2021-08-22	59448	IRDIS	-203.6	8.0	7.5	7.1	203.7	8.0	272.1	2.0	[10]
<i>c</i>	2021-09-02	59459	IRDIS	-207.0	6.0	11.0	7.2	207.3	6.0	273.2	2.0	[10]
<i>c</i>	2022-02-28	59638	IRDIS	-195.6	9.0	19	10	196.5	9.0	275.5	3.0	[10]
<i>c</i>	2023-02-24	59999	NIRISS	-221.1	8.7	-1.5	5.4	221.1	8.7	269.6	1.4	[8]
<i>c</i>	2023-03-08	60011	MagAO-X	-206.5	1.0	0.0	1.0	206.5	1.0	270.0	0.25	[11]
<i>c</i>	2023-03-08	60011	NIRCam	-196	23	-1	23	195.7	23.3	269.7	6.8	[9]
<i>c</i>	2024-03-25	60394	MagAO-X	-206.4	3.0	-7.2	1.8	206.55	3.0	268.0	0.50	[11]
<i>d</i>	2014-05-10	56787	SINFONI	-23.0	9.2	114.9	12.4	117.2	12.5	348.7	4.4	[12]
<i>d</i>	2016-06-01	57540	IFS	-49.0	22.3	103.3	18.4	114.3	17.1	334.6	11.7	[12]
<i>d</i>	2018-02-25	58174	IFS	-79.3	5.8	87.2	5.8	117.9	6.0	317.7	2.7	[12]
<i>d</i>	2019-03-06	58548	IFS	-84.1	7.3	86.2	7.3	120.4	8.3	315.7	2.9	[12]
<i>d</i>	2021-05-17	59351	IFS	-86.3	11.5	55.2	10.7	102.4	12.1	302.6	5.6	[12]
<i>d</i>	2021-08-21	59447	IFS	-89.9	12.7	64.6	12.6	110.7	12.7	305.7	6.5	[12]
<i>d</i>	2021-09-03	59460	IFS	-92.4	10.9	52.7	11.3	106.4	10.7	299.7	6.2	[12]
<i>d</i>	2022-02-28	59638	IFS	-95.2	6.7	53.7	7.2	109.3	6.5	299.4	3.9	[12]
<i>d</i>	2023-03-08	60011	NIRCam	-95	23	40	23	103.4	23.2	293.0	12.7	[9]

Notes. References: [1] [Keppler et al. \(2018\)](#); [2] [Müller et al. \(2018\)](#); [3] [Christiaens et al. \(2019\)](#); [4] [Haffert et al. \(2019\)](#); [5] [Mesa et al. \(2019\)](#); [6] [Wang et al. \(2020\)](#); [7] [Wang et al. \(2021\)](#); [8] [Blakely et al. \(2024\)](#); [9] [Christiaens et al. \(2024\)](#); [10] [Wahhaj et al. \(2024\)](#); [11] [Close et al. \(2025\)](#); [12] [Hammond et al. \(2025\)](#); [13] This work.

Appendix C: Corner Plots of Planet Orbital Parameters

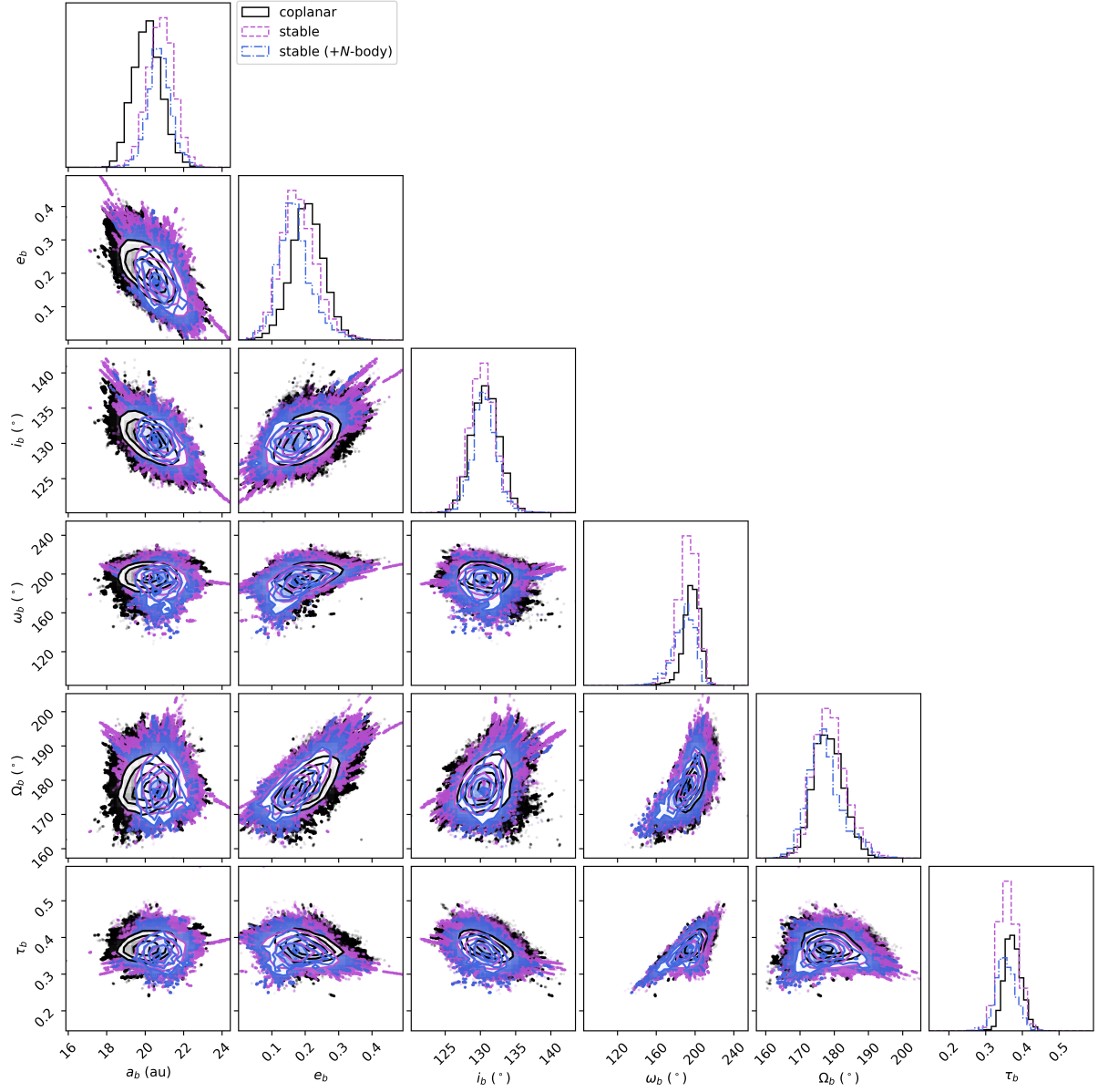


Fig. C.1. Corner plot of the posteriors for the orbital parameters of PDS 70 *b* from all MCMC orbital parameter fits to astrometry of PDS 70 *b* and *c* only. Posteriors from the fit assuming coplanarity are shown in black (solid lines). Posteriors from the fit assuming stability are shown both before (purple, dashed lines) and after (blue, dashed and dotted lines) *N*-body stability analysis.

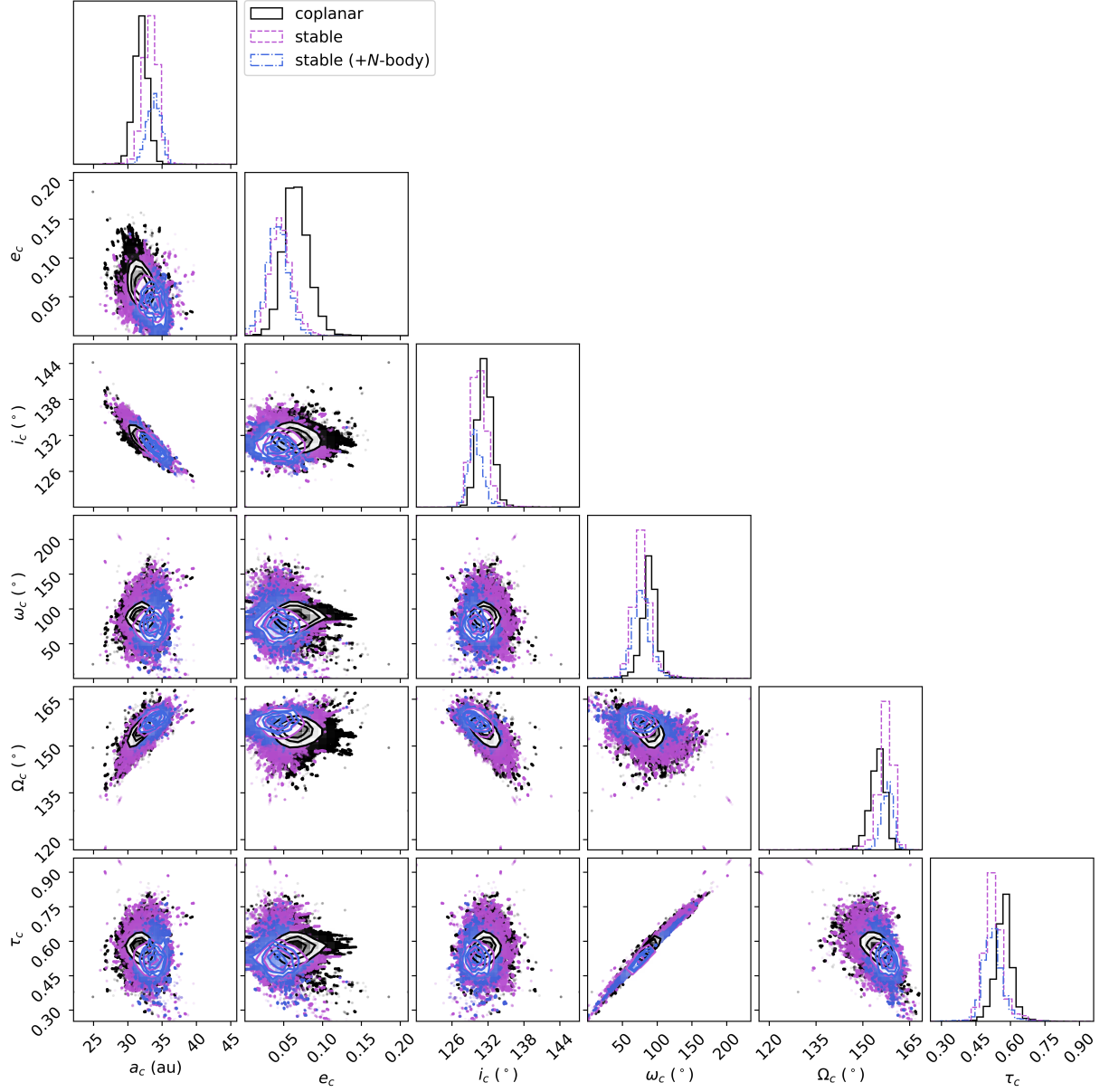


Fig. C.2. Corner plot of the posteriors for the orbital parameters of PDS 70 *c* from all MCMC orbital parameter fits to astrometry of PDS 70 *b* and *c* only. Posteriors from the fit assuming coplanarity are shown in black (solid lines). Posteriors from the fit assuming stability are shown both before (purple, dashed lines) and after (blue, dashed and dotted lines) *N*-body stability analysis.

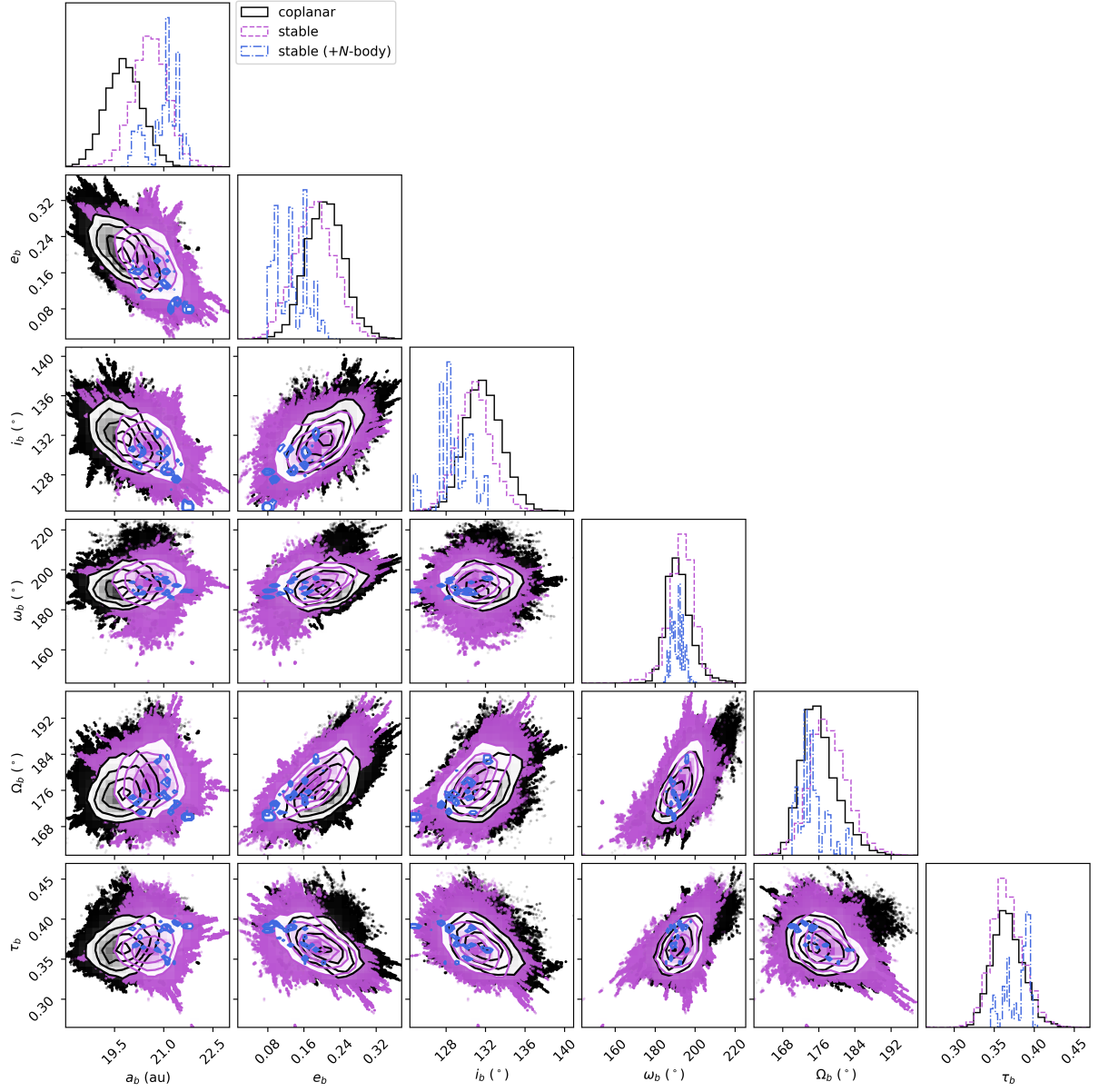


Fig. C.3. Corner plot of the posteriors for the orbital parameters of PDS 70 *b* from all MCMC orbital parameter fits to astrometry of PDS 70 *b*, *c* and *d*. Posteriors from the fit assuming coplanarity are shown in black (solid lines). Posteriors from the fit assuming stability are shown both before (purple, dashed lines) and after (blue, dashed and dotted lines) *N*-body stability analysis.

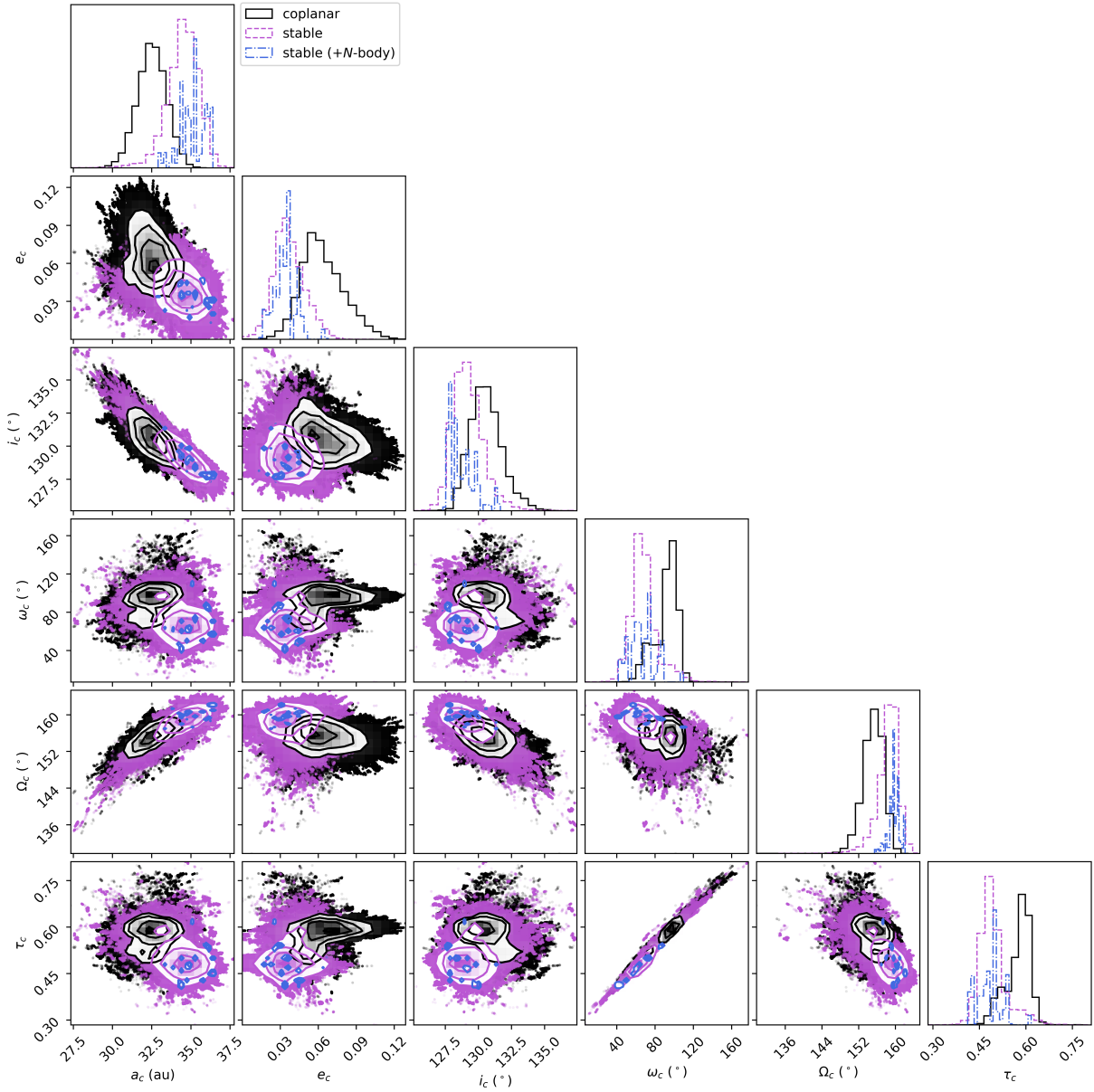


Fig. C.4. Corner plot of the posteriors for the orbital parameters of PDS 70 *c* from all MCMC orbital parameter fits to astrometry of PDS 70 *b*, *c* and *d*. Posteriors from the fit assuming coplanarity are shown in black (solid lines). Posteriors from the fit assuming stability are shown both before (purple, dashed lines) and after (blue, dashed and dotted lines) *N*-body stability analysis.

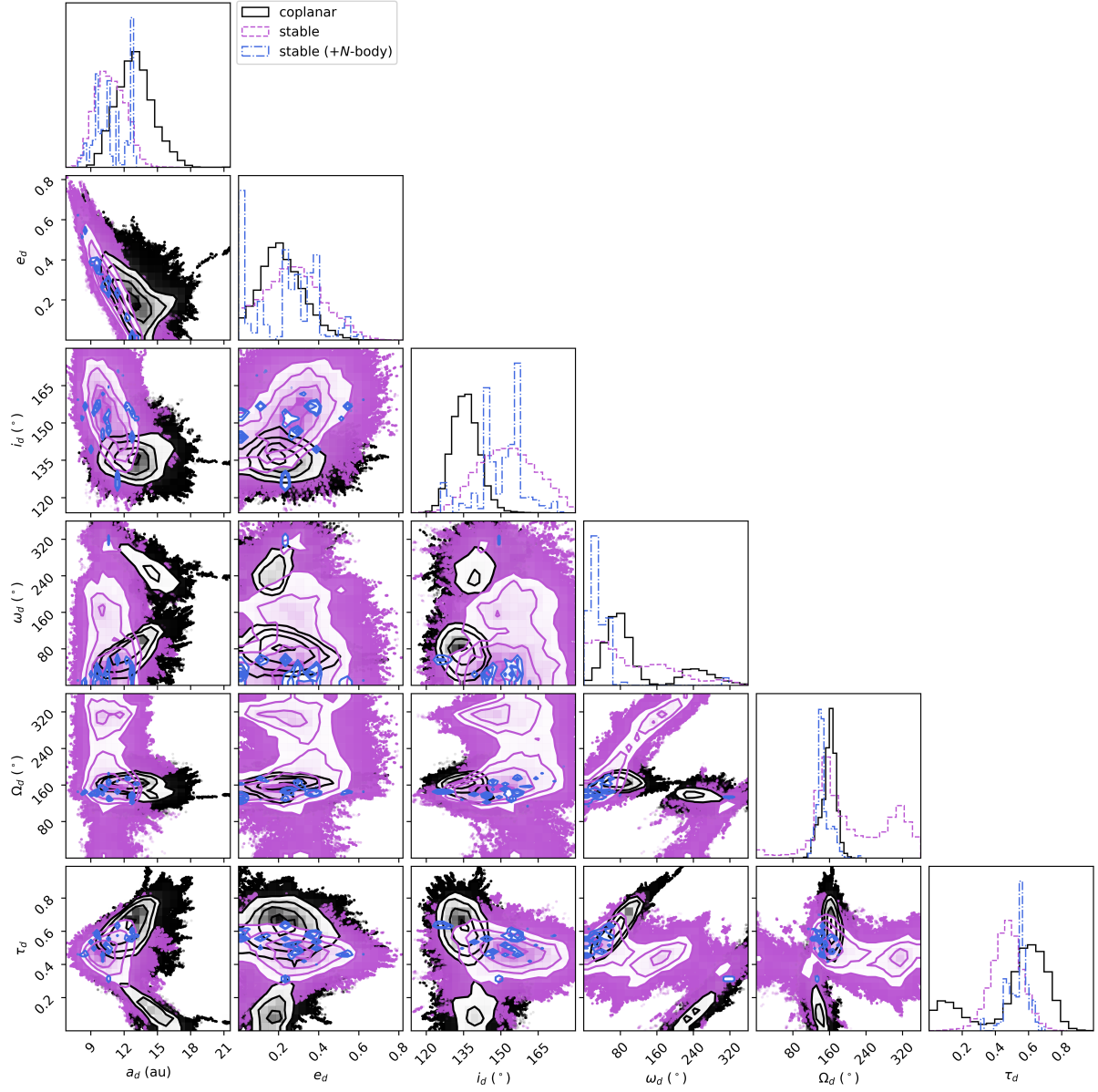


Fig. C.5. Corner plot of the posteriors for the orbital parameters of PDS 70 *d* from all MCMC orbital parameter fits to astrometry of PDS 70 *b*, *c* and *d*. Posteriors from the fit assuming coplanarity are shown in black (solid lines). Posteriors from the fit assuming stability are shown both before (purple, dashed lines) and after (blue, dashed and dotted lines) *N*-body stability analysis.